Mechanics of Advanced Materials and Structures

ISSN: (Print) (Online) Journal homepage: www.tandfonline.com/journals/umcm20

Application of machine learning algorithm and Carrera unified formulation in thermal buckling analysis of a functionally graded graphene origami enabled auxetic metamaterial sandwich plate with an auxetic concrete foundation

Qiang Lu, Qing Yang, M. Atif & Mohammed El-Meligy

To cite this article: Qiang Lu, Qing Yang, M. Atif & Mohammed El-Meligy (09 Nov 2024): Application of machine learning algorithm and Carrera unified formulation in thermal buckling analysis of a functionally graded graphene origami enabled auxetic metamaterial sandwich plate with an auxetic concrete foundation, Mechanics of Advanced Materials and Structures, DOI: 10.1080/15376494.2024.2423913

To link to this article: https://doi.org/10.1080/15376494.2024.2423913

Published online: 09 Nov 2024.

MECHANICS OF ADVANCED MATERIALS AND STRUCTURES
https://doi.org/10.1080/15376494.2024.2423913

ORIGINAL ARTICLE

Application of machine learning algorithm and Carrera unified formulation in thermal buckling analysis of a functionally graded graphene origami enabled auxetic metamaterial sandwich plate with an auxetic concrete foundation

Qiang Lu[a], Qing Yang[a], M. Atif[b], and Mohammed El-Meligy[c,d]

[a]School of Civil Engineering, Chongqing Vocational Institute of Engineering, Chongqing, China; [b]Department of Physics and Astronomy, College of Science, King Saud University, Riyadh, Saudi Arabia; [c]MEU Research Unit, Middle East University, Amman, Jordan; [d]Jadara University Research Center, Jadara University, Irbid, Jordan

ABSTRACT
This study presents a comprehensive thermal buckling analysis of sandwich plates composed of functionally graded graphene origami-enabled auxetic metamaterial (FG-GOEAM) face sheets on an auxetic concrete foundation, using Carrera's unified formulation (CUF) as the theoretical framework. FG-GOEAM materials are emerging as advanced composites, combining exceptional mechanical resilience, tunable auxetic behavior, and high thermal stability, making them suitable for extreme environments. By employing CUF, a powerful and adaptable modeling approach, this work accurately captures the complex mechanical interactions within the FG-GOEAM sandwich structure under thermal loads, incorporating both material gradation and auxetic properties. To further enhance the precision and efficiency of this thermal buckling analysis, a deep neural network (DNN) is developed as a machine learning algorithm to predict critical temperature differences, based on a dataset generated through mathematics simulation. The DNN model demonstrates excellent predictive capability, validated by close alignment between its estimates and CUF results, thus reducing computational costs while maintaining high accuracy. Parametric studies are conducted to assess the effects of material gradation, aspect ratios, and foundation properties on thermal buckling performance. The results highlight the superior thermal stability of FG-GOEAM structures and the potential of DNNs to serve as reliable, computationally efficient tools for advanced structural analysis. This study provides a novel, integrated framework for high-fidelity thermal buckling prediction in complex auxetic composites, paving the way for broader applications in engineering fields requiring lightweight, thermally stable structures.

ARTICLE HISTORY
Received 15 July 2024
Accepted 28 October 2024

KEYWORDS
Carrera unified formulation; thermal buckling; FG-GOEAM face sheets; auxetic concrete foundation; machine learning algorithm

1. Introduction

Composite structures are engineered materials made from two or more constituent materials with different physical or chemical properties, which remain distinct within the finished structure [1–3]. The combination of these materials creates a product with enhanced performance characteristics compared to the individual components [4, 5]. Typically, composites consist of a matrix material (like a polymer, metal, or ceramic) reinforced with fibers or particles that provide added strength and stiffness [6, 7]. One of the most common types of composites is fiber-reinforced polymer (FRP), which incorporates materials like carbon fiber or glass fiber within a polymer matrix, widely used in aerospace, automotive, and sports equipment [8–10]. Composites are valued for their high strength-to-weight ratios, corrosion resistance, and design flexibility, making them ideal for applications requiring lightweight and durable materials [11–13]. Advanced composites, like those with carbon nanotubes or graphene, offer even greater mechanical and thermal properties, expanding their use in high-performance engineering fields [14, 15]. The performance of composite structures is largely dependent on the type, orientation, and distribution of the reinforcement material within the matrix. In functionally graded composites, the material composition varies continuously across the structure, providing tailored properties that address specific mechanical, thermal, or acoustic needs [16, 17]. Recent developments in auxetic materials—materials with a negative Poisson's ratio—have led to composites that expand laterally under tension, providing unique mechanical advantages, such as increased energy absorption [18]. Sandwich structures, which use lightweight core materials sandwiched between stiffer face sheets, are a common composite design in structural applications where both strength and low weight are critical [16]. In aerospace and civil engineering, composite structures are increasingly replacing traditional materials like metals due to their superior performance under dynamic and thermal loads [19]. However, the complexity of composite materials necessitates advanced analytical and computational methods to accurately predict their behavior under various conditions

CONTACT Qing Yang raricsxj@163.com School of Civil Engineering, Chongqing Vocational Institute of Engineering, Chongqing, 402260, China.

[20]. Recent advancements in machine learning and neural networks have shown promise in modeling the complex behaviors of composites, reducing the computational effort required in traditional simulations [21]. As composite materials continue to evolve, they are expected to play a central role in sustainable engineering solutions, offering lightweight, strong, and environmentally resilient alternatives for modern infrastructure and transportation [22, 23].

The CUF is essential for engineers as it provides a versatile framework to analyze complex structural behaviors within a single, unified approach [24]. CUF enables engineers to address various structural theories (e.g. classical and higher-order) seamlessly, which is especially valuable in handling multi-layered composites and advanced materials [25]. It allows engineers to model the intricate stress and deformation patterns in layered structures like sandwich panels, widely used in aerospace and automotive industries [26]. By accommodating higher-order theories, CUF offers greater accuracy in capturing localized effects that traditional models may miss, such as interlaminar stresses in composites [27]. For engineers, CUF's computational efficiency means they can achieve accurate results without excessive processing time, making it suitable for large-scale simulations [28]. Its adaptability to different boundary conditions and load types enables engineers to apply it to a variety of structural scenarios, from thermal buckling to dynamic loading [29]. Additionally, CUF facilitates the optimization of materials and structures, allowing engineers to design lightweight, efficient, and resilient components [30]. With the rise of functionally graded and auxetic materials, CUF's ability to model graded properties is crucial [30]. Overall, CUF empowers engineers to conduct high-fidelity structural analyses, leading to safer, more optimized designs [31].

Modeling plays a crucial role in engineering, providing numerous benefits that enhance the design, analysis, and implementation of projects [32, 33]. First, it allows engineers to visualize complex systems and components before physical construction, enabling better understanding and communication [34, 35]. By creating models, engineers can explore various design alternatives quickly, assessing their feasibility and performance [36, 37]. This iterative process leads to optimized solutions, reducing time and costs [38, 39]. Additionally, modeling helps in predicting the behavior of systems under different conditions, which is essential for risk management and safety assessment [40, 41]. Engineers can simulate real-world scenarios, enabling them to identify potential issues and make necessary adjustments [42, 43]. This proactive approach enhances product reliability and longevity [44, 45]. Furthermore, modeling supports interdisciplinary collaboration by providing a common framework for different engineering specialties to work together [46, 47]. Engineers can use models to share insights and integrate their knowledge, leading to more holistic solutions [48, 49]. In the context of software development, modeling facilitates the development of algorithms and systems architecture, ensuring that all components interact seamlessly [50, 51]. Modeling also aids in documentation and compliance with industry standards, providing clear records of design decisions and processes [52, 53]. This transparency is crucial for regulatory approvals and quality assurance [54, 55]. Moreover, it enhances the learning process for engineers, allowing them to experiment and learn from their models without the risks associated with real-world testing [56, 57]. Finally, as industries increasingly adopt digital transformation, modeling becomes vital for integrating emerging technologies like artificial intelligence and machine learning into engineering practices [58]. Ref. [59] provided a data-driven methodology for identifying distinct consumer profiles, enabling financial institutions to enhance targeted strategies that support economic stability and mitigate credit risk. Extreme value mixture modeling has emerged as a robust approach for estimating tail risk measures in finance, blending extreme value theory (EVT) with distributional modeling to better capture the probability and impact of rare, high-magnitude financial losses, thereby enhancing risk management and stress testing practices [60].

Using CUF as the theoretical basis, this research provides a thorough thermal buckling analysis of sandwich plates made of FG-GOEAM face sheets on an auxetic concrete substrate. With their remarkable mechanical robustness, adjustable auxetic activity, and great thermal stability, FG-GOEAM materials are becoming cutting-edge composites that can withstand harsh conditions. This study effectively depicts the intricate mechanical interactions inside the FG-GOEAM sandwich structure under thermal stresses by using CUF, a potent and versatile modeling technique that incorporates both material gradation and auxetic features. Based on a dataset produced by mathematics simulation, a DNN is created as a machine learning technique to anticipate crucial temperature variations to further improve the accuracy and effectiveness of this thermal buckling study. Close congruence between the DNN model's estimations and CUF findings confirms its exceptional predictive abilities, which lowers computing costs without sacrificing accuracy. To evaluate how foundation characteristics, aspect ratios, and material gradation affect thermal buckling performance, parametric tests are carried out. The findings demonstrate both the potential of DNNs to be dependable, computationally effective tools for advanced structural analysis and the enhanced thermal stability of FG-GOEAM systems. This work opens the door for wider applications in engineering domains needing lightweight, thermally stable structures by offering a unique, comprehensive framework for high-fidelity thermal buckling prediction in complex auxetic composites.

2. Mathematical modeling

2.1. Effective material properties

A copper core and graphene origami-enabled auxetic metamaterial face sheets make up the sandwich plate sitting on the auxetic foundation, as shown in Figure 1, along with the corresponding measurements.

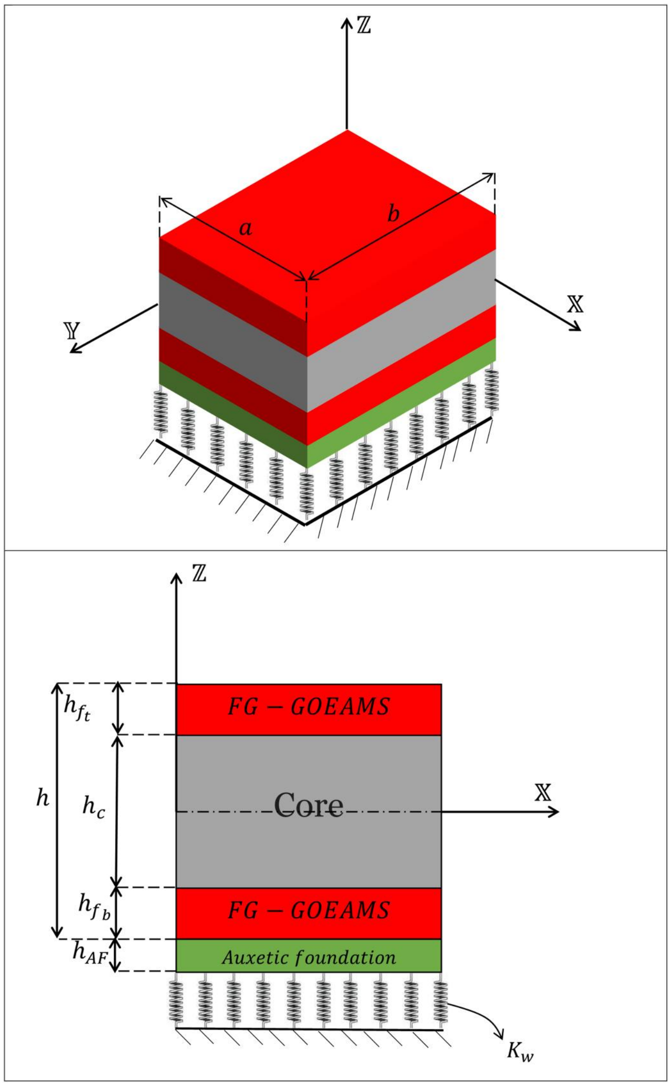

Figure 1. Schematic of sandwich plate resting on auxetic foundation.

2.1.1. Graphene origami-enabled auxetic metamaterial face sheets

Figure 2 illustrates how the FG-GOEAM composite plates are built with differences in GOri content and GOri folding degree. The two patterns in Figure 2 illustrate how the GOri content changes layer by layer in the thickness direction. Greater GOri concentration is indicated by a deeper hue, and the weight fraction (W_{Gr}) varies in proportion. The U-W_{Gr} pattern indicates a homogeneous, isotropic metamaterial plate with GOri evenly distributed across each layer. The distribution of the X-W_{Gr} pattern is symmetrical, and the outer surface layers have a larger proportion of GOri. Furthermore, the H atom coverage (H_{Gr}) in the crease, which indicates the folding degree of GOri, is thought to progressively alter in the direction of thickness. A greater value denotes a greater amount of hydrogen atoms that are chemically connected to the GOri folds, increasing the folding degree. The two different folding degree patterns of GOri that are examined in this work are U-H_{Gr} and X-H_{Gr}, as seen in Figure 2. Whereas the X-H_{Gr} pattern depicts an FG metamaterial plate with pristine graphene scattered on the surfaces and GOri scattered in the center, the U-H_{Gr} pattern depicts an isotropic homogenous metamaterial plate.

For the two graphene content distribution patterns, the volume percentages of the k-th layer, or $V_{\mathrm{Gr}}(k)$, are controlled by [61]

$$\begin{aligned} &U-W_{\mathrm{Gr}}: V_{\mathrm{Gr}}(k)=V_{\mathrm{Gr}},\\ &X-W_{\mathrm{Gr}}: V_{\mathrm{Gr}}(k)=2V_{\mathrm{Gr}}|2k-N_L-1|/N_L, \end{aligned} \tag{1}$$

where N_L is the total number of layers and k is between 1 and N_L. The weight fraction W_{Gr} may be converted to the volume fraction V_{Gr}.

$$\begin{aligned} &V_{\mathrm{Gr}}=\frac{\rho_{\mathrm{Cu}}W_{\mathrm{Gr}}}{\rho_{\mathrm{Cu}}W_{\mathrm{Gr}}+\rho_{\mathrm{Gr}}(1-W_{\mathrm{Gr}})},\\ &V_{\mathrm{Gr}}+V_{\mathrm{Cu}}=1, \end{aligned} \tag{2}$$

where ρ_{Cu} and ρ_{Gr} are the volume fraction of copper and the densities of pure copper and graphene, respectively. Both a uniform and a non-uniform distribution along the thickness direction produce the H coverages $H_{\mathrm{Gr}}(\mathbb{Z})$.

$$\begin{aligned} &U-H_{\mathrm{Gr}}: H_{\mathrm{Gr}}(\mathbb{Z})=H_{\mathrm{Gr}}, \text{Face-sheet top}\\ &U-H_{\mathrm{Gr}}: H_{\mathrm{Gr}}(\mathbb{Z})=H_{\mathrm{Gr}}, \text{Face-sheet bottom}\\ &X-H_{\mathrm{Gr}}: H_{\mathrm{Gr}}(\mathbb{Z})=H_{\mathrm{Gr}}\cos\left(\frac{\mathbb{Z}-0.5h_c-0.5h_{f_b}}{h_{f_b}}\pi\right),\\ &\qquad \text{Face-sheet top}\\ &X-H_{\mathrm{Gr}}: H_{\mathrm{Gr}}(\mathbb{Z})=H_{\mathrm{Gr}}\cos\left(\frac{\mathbb{Z}+0.5h_c+0.5h_{f_t}}{h_{f_t}}\pi\right),\\ &\qquad \text{Face-sheet bottom} \end{aligned} \tag{3}$$

The material characteristics of GOEAMs, including the Poisson's ratio (ν), Young's modulus (E), and thermal expansion (α), are calculated using GP-assisted micromechanical models [61]:

$$\begin{aligned} &E_j=\frac{1+\xi\eta V_{\mathrm{Gr}}}{1-\eta V_{\mathrm{Gr}}}E_{\mathrm{Cu}}\times f_E(H_{\mathrm{Gr}},V_{\mathrm{Gr}},T),\\ &\nu_j=(\nu_{\mathrm{Gr}}V_{\mathrm{Gr}}+\nu_{\mathrm{Cu}}V_{\mathrm{Cu}})\times f_\nu(H_{\mathrm{Gr}},V_{\mathrm{Gr}},T),\\ &\alpha_j=(\alpha_{\mathrm{Gr}}V_{\mathrm{Gr}}+\alpha_{\mathrm{Cu}}V_{\mathrm{Cu}})\times f_\alpha(V_{\mathrm{Gr}},T), \end{aligned} \tag{4}$$

When j equals f_b and f_t. The coefficient of material (η) and size (ξ) are stated as follows:

$$\begin{aligned} &\eta=\frac{(E_{\mathrm{Gr}}/E_{\mathrm{Cu}})-1}{(E_{\mathrm{Gr}}/E_{\mathrm{Cu}})+\xi},\\ &\xi=2(l_{\mathrm{Gr}}/t_{\mathrm{Gr}}), \end{aligned} \tag{5}$$

where l_{Gr} and t_{Gr} stand for graphene's length and thickness, respectively; the modification functions $f_{E,\nu,\alpha}(H_{\mathrm{Gr}},V_{\mathrm{Gr}},T)$ are derived using the GP method, which is expressed as [62].

$$\begin{aligned} &f_E(H_{\mathrm{Gr}},V_{\mathrm{Gr}},T)=1.11-1.22V_{\mathrm{Gr}}-0.134\left(\frac{T}{T_0}\right)+0.559V_{\mathrm{Gr}}\left(\frac{T}{T_0}\right)\\ &\quad -5.5H_{\mathrm{Gr}}V_{\mathrm{Gr}}+38H_{\mathrm{Gr}}V_{\mathrm{Gr}}^2-20.6H_{\mathrm{Gr}}^2V_{\mathrm{Gr}}^2,\\ &f_\nu(H_{\mathrm{Gr}},V_{\mathrm{Gr}},T)=1.01-1.43V_{\mathrm{Gr}}+0.165\left(\frac{T}{T_0}\right)-16.8H_{\mathrm{Gr}}V_{\mathrm{Gr}}\\ &\quad -1.1H_{\mathrm{Gr}}V_{\mathrm{Gr}}\left(\frac{T}{T_0}\right)+16H_{\mathrm{Gr}}^2V_{\mathrm{Gr}}^2,\\ &f_\alpha(V_{\mathrm{Gr}},T)=0.794-16.8V_{\mathrm{Gr}}^2-0.0279\left(\frac{T}{T_0}\right)^2\\ &\quad +0.182\left(\frac{T}{T_0}\right)(1+V_{\mathrm{Gr}}). \end{aligned} \tag{6}$$

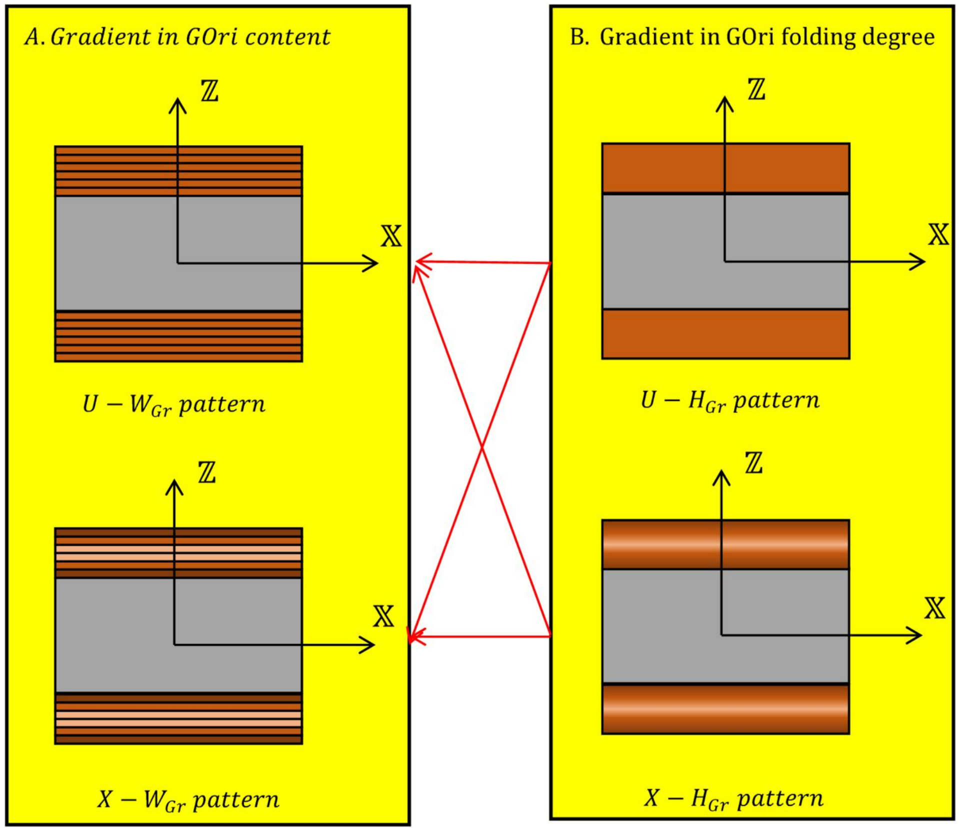

Figure 2. Sandwich plate with gradients in (A) graphene content and (B) graphene folding degree.

In which $T_0 = 300$ K and T is the ambient temperature [62]. The following are the relevant material properties of Cu unless otherwise noted: At 300 K, the coefficient of thermal expansion (α_{Cu}) is 16.51×10^{-6} K^{-1}, the Young's modulus (E_{Cu}) is 65.79 GPa, and the Poisson's ratio (ν_{Cu}) is 0.387. At a temperature of 300 K, graphene's coefficient of thermal expansion (α_{Cu}) is -3.98×10^{-6} K^{-1}, its elastic modulus (E_{GR}) is 929.57 GPa, and its Poisson's ratio (ν_{GR}) is 0.220. The graphene is 3.4 Å thick and 83.76 Å long geometrically.

3. FEM analysis based on CUF

The separation of variables in mathematics is comparable to CUF in FEM. Accordingly, the displacement vector is a function of $\mathbb{X}, \mathbb{Y}, \mathbb{Z}$ divided into the expansion function ($\mathfrak{U}_\tau$) and the shape function (N_i). Shape functions interpolate the displacement components at the mid-surface of the plate and are believed to be connected to in-plane coordinates $\mathbb{X}$ and $\mathbb{Y}$, while expansion functions interpolate the displacement components together with the plate thickness and solely depend on out-of-plane coordinate $\mathbb{Z}$. Consequently, an element's displacement field $\boldsymbol{u} = [u_\mathbb{X}, u_\mathbb{Y}, u_\mathbb{Z}]^T$ may be written as follows:

$$\boldsymbol{u} = \mathfrak{U}_\tau(\mathbb{Z}) N_i(\mathbb{X}, \mathbb{Y}) \boldsymbol{u}_{\tau i}. \tag{7}$$

in which $\boldsymbol{u}_{\tau i} = [u_{\mathbb{X}_{\tau i}}, u_{\mathbb{Y}_{\tau i}}, u_{\mathbb{Z}_{\tau i}}]^T$. The subscript $i = 1, 2, ..., w$ denotes the element node and w represents the number of nodes per element, whereas the subscript $\tau = 1, 2, ..., m$ denotes the expansion function and m represents the number of expansion functions used per node. T is a vector of nodal generalized coordinates. Taylor-like functions have been used as expansion functions in this article in the following ways:

$$\mathfrak{U}_\tau(\mathbb{Z}) = \mathbb{Z}^{\tau - 1}. \tag{8}$$

The shape functions in FEM, which are derived from the Lagrange polynomials, have been used in this instance in their customary forms. This element has nine nodes and the shape functions shown below:

$$\mathfrak{H}_1 = \frac{1}{4}(\mathbb{A}^2 - \mathbb{A})(\mathbb{B}^2 - \mathbb{B}), \tag{9a}$$

$$\mathfrak{H}_2 = \frac{1}{2}(1 - \mathbb{A}^2)(\mathbb{B}^2 - \mathbb{B}), \tag{9b}$$

$$\mathfrak{H}_3 = \frac{1}{4}(\mathbb{A}^2 + \mathbb{A})(\mathbb{B}^2 - \mathbb{B}), \tag{9c}$$

$$\mathfrak{H}_4 = \frac{1}{2}(1 - \mathbb{B}^2)(\mathbb{A}^2 + \mathbb{A}), \tag{9d}$$

$$\mathfrak{H}_5 = \frac{1}{4}(\mathbb{A}^2 + \mathbb{A})(\mathbb{B}^2 + \mathbb{B}), \tag{9e}$$

$$\mathfrak{H}_6 = \frac{1}{2}(1 - \mathbb{A}^2)(\mathbb{B}^2 + \mathbb{B}), \tag{9f}$$

$$\mathfrak{H}_7 = \frac{1}{4}(\mathbb{A}^2 - \mathbb{A})(\mathbb{B}^2 + \mathbb{B}), \tag{9g}$$

$$\mathfrak{H}_8 = \frac{1}{2}(1 - \mathbb{B}^2)(\mathbb{A}^2 - \mathbb{A}), \tag{9h}$$

$$\mathfrak{H}_9 = (1 - \mathbb{A}^2)(1 - \mathbb{B}^2). \tag{9i}$$

where $\mathbb{A}$, and $\mathbb{B}$ are natural coordinates that fall inside the interval $[-1, 1]$. The rectangular elements will be employed in the finite element mesh as the rectangular plates are the only ones taken into consideration in this work.

3.1. Governing equations

This concept states that the structure's overall virtual work variation must be zero. As stated otherwise, there is no difference between the external work variation $\delta\mathfrak{L}_{\text{ext}}$ and the virtual internal work variation $\delta\mathfrak{L}_{\text{int}}$

$$\delta\mathfrak{L}_{\text{int}} - \delta\mathfrak{L}_{\text{ext}} = 0. \tag{10}$$

The virtual internal work $\delta\mathfrak{L}_{\text{int}}$ is separated into two halves in this study, and there is no external work.

$$\delta\mathfrak{L}_{int} = \delta\mathfrak{L}_{I} + \delta\mathfrak{L}_{II} + \delta\mathfrak{L}_{III}. \tag{11}$$

The following is the first section of virtual internal work:

$$\delta\mathfrak{L}_{I} = \int_{V_e} \delta\boldsymbol{\mathcal{E}}_{l}^{T}\mathfrak{Y}\,\mathrm{d}V. \tag{12}$$

where linear strain and stress vectors are denoted by $\mathfrak{Y}$ and $\boldsymbol{\mathcal{E}}_{l}$, respectively. They are described as:

$$\mathfrak{Y} = [\mathfrak{Y}_{\mathbb{XX}}, \mathfrak{Y}_{\mathbb{YY}}, \mathfrak{Y}_{\mathbb{ZZ}}, \mathfrak{Y}_{\mathbb{XZ}}, \mathfrak{Y}_{\mathbb{YZ}}, \mathfrak{Y}_{\mathbb{XY}}]^{\mathrm{T}}, \tag{13a}$$

$$\mathcal{E}_{l} = [\mathcal{E}_{\mathbb{XX}}, \mathcal{E}_{\mathbb{YY}}, \mathcal{E}_{\mathbb{ZZ}}, \mathcal{E}_{\mathbb{XZ}}, \mathcal{E}_{\mathbb{YZ}}, \mathcal{E}_{\mathbb{XY}}]^{\mathrm{T}}. \tag{13b}$$

In Eqs. (13a) and (13b), according to Hooke's law the stress vector $\mathfrak{Y}$ can be connect with linear strain vector $\mathcal{E}_{l}$ by a matrix defined as:

$$\begin{Bmatrix} \mathfrak{Y}_{\mathbb{XX}} \\ \mathfrak{Y}_{\mathbb{YY}} \\ \mathfrak{Y}_{\mathbb{ZZ}} \\ \mathfrak{Y}_{\mathbb{XZ}} \\ \mathfrak{Y}_{\mathbb{YZ}} \\ \mathfrak{Y}_{\mathbb{XY}} \end{Bmatrix} = \begin{bmatrix} \mathcal{T}_{11} & \mathcal{T}_{12} & \mathcal{T}_{13} & 0 & 0 & 0 \\ \mathcal{T}_{12} & \mathcal{T}_{22} & \mathcal{T}_{23} & 0 & 0 & 0 \\ \mathcal{T}_{13} & \mathcal{T}_{23} & \mathcal{T}_{33} & 0 & 0 & 0 \\ 0 & 0 & 0 & \mathcal{T}_{66} & 0 & 0 \\ 0 & 0 & 0 & 0 & \mathcal{T}_{55} & 0 \\ 0 & 0 & 0 & 0 & 0 & \mathcal{T}_{44} \end{bmatrix} \begin{Bmatrix} \varepsilon_{\mathbb{XX}} \\ \varepsilon_{\mathbb{YY}} \\ \varepsilon_{\mathbb{ZZ}} \\ \mathcal{E}_{\mathbb{XZ}} \\ \mathcal{E}_{\mathbb{YZ}} \\ \mathcal{E}_{\mathbb{XY}} \end{Bmatrix}. \tag{14}$$

The coefficients $\mathcal{T}_{ij}$ are known in terms of Young modulus and Poisson ratio of the kth layer as below:

For face-sheets have:

$$\begin{aligned} &\mathcal{T}_{11f_b} = \frac{E_{f_b}(1-\nu_{f_b})}{(1+\nu_{f_b})(1-2\nu_{f_b})}, \mathcal{T}_{33f_b} = \mathcal{T}_{22f_b} = \mathcal{T}_{11f_b}, \\ &\mathcal{T}_{12f_b} = \frac{E_{f_b}\nu_{f_b}}{(1+\nu_{f_b})(1-2\nu_{f_b})}, \mathcal{T}_{13f_b} = \mathcal{T}_{23f_b} = \mathcal{T}_{12f_b}, \\ &\mathcal{T}_{44f_b} = \frac{E_{f_b}}{2(1+\nu_{f_b})}, \mathcal{T}_{55f_b} = \mathcal{T}_{55f_b} = \mathcal{T}_{44f_b}. \\ &\mathcal{T}_{11f_t} = \frac{E_{f_t}(1-\nu_{f_t})}{(1+\nu_{f_t})(1-2\nu_{f_t})}, \mathcal{T}_{33f_t} = \mathcal{T}_{22f_t} = \mathcal{T}_{11f_t}, \\ &\mathcal{T}_{12f_t} = \frac{E_{f_t}\nu_{f_t}}{(1+\nu_{f_t})(1-2\nu_{f_t})}, \mathcal{T}_{13f_t} = \mathcal{T}_{23f_t} = \mathcal{T}_{12f_t}, \\ &\mathcal{T}_{44f_t} = \frac{E_{f_t}}{2(1+\nu_{f_t})}, \mathcal{T}_{66f_t} = \mathcal{T}_{55f_t} = \mathcal{T}_{44f_t}. \end{aligned} \tag{15}$$

For core have:

$$\begin{aligned} &\mathcal{T}_{11c} = \frac{E_{C\mathscr{u}}(1-\nu_{C\mathscr{u}})}{(1+\nu_{C\mathscr{u}})(1-2\nu_{C\mathscr{u}})}, \mathcal{T}_{33c} = \mathcal{T}_{22c} = \mathcal{T}_{11c}, \\ &\mathcal{T}_{12c} = \frac{E_{C\mathscr{u}}\nu_{C\mathscr{u}}}{(1+\nu_{C\mathscr{u}})(1-2\nu_{C\mathscr{u}})}, \mathcal{T}_{13c} = \mathcal{T}_{23c} = \mathcal{T}_{12c}, \\ &\mathcal{T}_{44c} = \frac{E_{C\mathscr{u}}}{2(1+\nu_{C\mathscr{u}})}, \mathcal{T}_{66c} = \mathcal{T}_{55c} = \mathcal{T}_{44c}. \end{aligned} \tag{16}$$

Linear strain vector is related to the displacement vector by an operator as below:

$$\boldsymbol{\mathcal{E}}_{l} = D\boldsymbol{u}_{\tau i}, \tag{17}$$

where

$$\mathbb{D} = \begin{bmatrix} \partial_{\mathbb{X}} & 0 & 0 \\ 0 & \partial_{\mathbb{Y}} & 0 \\ 0 & 0 & \partial_{\mathbb{Z}} \\ \partial_{\mathbb{Z}} & 0 & \partial_{\mathbb{X}} \\ 0 & \partial_{\mathbb{Z}} & \partial_{\mathbb{Y}} \\ \partial_{\mathbb{Y}} & \partial_{\mathbb{X}} & 0 \end{bmatrix}, \tag{18}$$

The variation of Eq. (17) is as follows:

$$\delta\mathcal{E}_{l} = \mathbb{D}\delta\boldsymbol{u}_{sj}, \tag{19}$$

The first section of virtual internal work for an element may be summed up as follows by replacing Eq. (17) in Eq. (14) and the resultant equation and Eq. (19) in Eq. (12)

$$\delta\mathfrak{L}_{I} = \delta\boldsymbol{u}_{sj}^{T}\mathbf{K}_{I}^{\tau sij}(T_1)\boldsymbol{u}_{\tau i}. \tag{20}$$

where $\mathbf{K}_{I}^{\tau sij}(T_1)$ is the element's first stiffness fundamental nucleus, and the Eqs. (21a)–(21i) defines its constituent parts. Note that although indices τ and s pertain to expansion functions, indexes i and j are maintained for element nodes in this article. T_1 stands for temperature in both this equation and this publication.

$$\begin{aligned} K_{\mathbb{XX}}^{\tau sij} = &\int \mathcal{T}_{55}\mathfrak{U}_{\tau,\mathbb{Z}}\mathfrak{U}_{s,\mathbb{Z}}d\mathbb{Z}\iint \mathfrak{H}_i\mathfrak{H}_j d\mathbb{X}d\mathbb{Y} \\ &+ \int \mathcal{T}_{11}\mathfrak{U}_{\tau}\mathfrak{U}_{s}d\mathbb{Z}\iint \mathfrak{H}_{i,\mathbb{X}}\mathfrak{H}_{j,\mathbb{X}}d\mathbb{X}d\mathbb{Y} \\ &+ \int \mathcal{T}_{66}\mathfrak{U}_{\tau}\mathfrak{U}_{s}d\mathbb{Z}\iint \mathfrak{H}_{i,\mathbb{Y}}\mathfrak{H}_{j,\mathbb{Y}}d\mathbb{X}d\mathbb{Y}, \end{aligned} \tag{21a}$$

$$\begin{aligned} K_{\mathbb{XY}}^{\tau sij} = &\int \mathcal{T}_{66}\mathfrak{U}_{\tau}\mathfrak{U}_{s}d\mathbb{Z}\iint \mathfrak{H}_{i,\mathbb{Y}}\mathfrak{H}_{j,\mathbb{X}}d\mathbb{X}d\mathbb{Y} \\ &+ \int \mathcal{T}_{12}\mathfrak{U}_{\tau}\mathfrak{U}_{s}d\mathbb{Z}\iint \mathfrak{H}_{i,\mathbb{X}}\mathfrak{H}_{j,\mathbb{Y}}d\mathbb{X}d\mathbb{Y}, \end{aligned} \tag{21b}$$

$$\begin{aligned} K_{\mathbb{XZ}}^{\tau sij} = &\int \mathcal{T}_{13}\mathfrak{U}_{\tau}\mathfrak{U}_{s,\mathbb{Z}}d\mathbb{Z}\iint \mathfrak{H}_{i,\mathbb{X}}\mathfrak{H}_{j}d\mathbb{X}d\mathbb{Y} \\ &+ \int \mathcal{T}_{55}\mathfrak{U}_{\tau,\mathbb{Z}}\mathfrak{U}_{s}d\mathbb{Z}\iint \mathfrak{H}_{i}\mathfrak{H}_{j,\mathbb{X}}d\mathbb{X}d\mathbb{Y}, \end{aligned} \tag{21c}$$

$$\begin{aligned} K_{\mathbb{YX}}^{\tau sij} = &\int \mathcal{T}_{12}\mathfrak{U}_{\tau}\mathfrak{U}_{s}d\mathbb{Z}\iint \mathfrak{H}_{i,\mathbb{Y}}\mathfrak{H}_{j,\mathbb{X}}d\mathbb{X}d\mathbb{Y} \\ &+ \int \mathcal{T}_{66}\mathfrak{U}_{\tau}\mathfrak{U}_{s}d\mathbb{Z}\iint \mathfrak{H}_{i,\mathbb{X}}\mathfrak{H}_{j,\mathbb{Y}}d\mathbb{X}d\mathbb{Y}, \end{aligned} \tag{21d}$$

$$\begin{aligned} K_{\mathbb{YY}}^{\tau sij} = &\int \mathcal{T}_{44}\mathfrak{U}_{\tau,\mathbb{Z}}\mathfrak{U}_{s,\mathbb{Z}}d\mathbb{Z}\iint \mathfrak{H}_{i}\mathfrak{H}_{j}d\mathbb{X}d\mathbb{Y} \\ &+ \int \mathcal{T}_{66}\mathfrak{U}_{\tau}\mathfrak{U}_{s}d\mathbb{Z}\iint \mathfrak{H}_{i,\mathbb{X}}\mathfrak{H}_{j,\mathbb{X}}d\mathbb{X}d\mathbb{Y} \\ &+ \int \mathcal{T}_{22}\mathfrak{U}_{\tau}\mathfrak{U}_{s}d\mathbb{Z}\iint \mathfrak{H}_{i,\mathbb{Y}}\mathfrak{H}_{j,\mathbb{Y}}d\mathbb{X}d\mathbb{Y}, \end{aligned} \tag{21e}$$

$$K_{\mathbb{YZ}}^{\tau sij} = \int \mathcal{T}_{23}\mathfrak{U}_{\tau}\mathfrak{U}_{s,\mathbb{Z}}d\mathbb{Z}\int\int \mathfrak{H}_{i,\mathbb{Y}}\mathfrak{H}_{j}d\mathbb{X}d\mathbb{Y} + \int \mathcal{T}_{44}\mathfrak{U}_{\tau,\mathbb{Z}}\mathfrak{U}_{s}d\mathbb{Z}\int\int \mathfrak{H}_{i}\mathfrak{H}_{j,\mathbb{Y}}d\mathbb{X}d\mathbb{Y}, \tag{21f}$$

$$K_{\mathbb{ZX}}^{\tau sij} = \int \mathcal{T}_{55}\mathfrak{U}_{\tau}\mathfrak{U}_{s,\mathbb{Z}}d\mathbb{Z}\int\int \mathfrak{H}_{i,\mathbb{X}}\mathfrak{H}_{j}d\mathbb{X}d\mathbb{Y} + \int \mathcal{T}_{13}\mathfrak{U}_{\tau,\mathbb{Z}}\mathfrak{U}_{s}d\mathbb{Z}\int\int \mathfrak{H}_{i}\mathfrak{H}_{j,\mathbb{X}}d\mathbb{X}d\mathbb{Y}, \tag{21g}$$

$$K_{\mathbb{ZY}}^{\tau sij} = \int \mathcal{T}_{44}\mathfrak{U}_{\tau}\mathfrak{U}_{s,\mathbb{Z}}d\mathbb{Z}\int\int \mathfrak{H}_{i,\mathbb{Y}}\mathfrak{H}_{j}d\mathbb{X}d\mathbb{Y} + \int \mathcal{T}_{23}\mathfrak{U}_{\tau,\mathbb{Z}}\mathfrak{U}_{s}d\mathbb{Z}\int\int \mathfrak{H}_{i}\mathfrak{H}_{j,\mathbb{Y}}d\mathbb{X}d\mathbb{Y}, \tag{21h}$$

$$K_{\mathbb{ZZ}}^{\tau sij} = \int \mathcal{T}_{55}\mathfrak{U}_{\tau}\mathfrak{U}_{s}d\mathbb{Z}\int\int \mathfrak{H}_{i,\mathbb{X}}\mathfrak{H}_{j,\mathbb{X}}d\mathbb{X}d\mathbb{Y} + \int \mathcal{T}_{44}\mathfrak{U}_{\tau}\mathfrak{U}_{s}d\mathbb{Z}\int\int \mathfrak{H}_{i,\mathbb{Y}}\mathfrak{H}_{j,\mathbb{Y}}d\mathbb{X}d\mathbb{Y} + \int \mathcal{T}_{33}\mathfrak{U}_{\tau,\mathbb{Z}}\mathfrak{U}_{s,\mathbb{Z}}d\mathbb{Z}\int\int \mathfrak{H}_{i}\mathfrak{H}_{j}d\mathbb{X}d\mathbb{Y}. \tag{21i}$$

The similar method has been used to calculate the second portion of the virtual internal work caused by in-plane pre-thermal stresses:

$$\delta\mathfrak{L}_{II} = \int_{V_e}\left(\delta\left\{\begin{matrix}\frac{1}{2}\left(u_{\mathbb{X},\mathbb{X}}^2 + u_{\mathbb{Y},\mathbb{X}}^2 + u_{\mathbb{Z},\mathbb{X}}^2\right)\\ \frac{1}{2}\left(u_{\mathbb{X},\mathbb{Y}}^2 + u_{\mathbb{Y},\mathbb{Y}}^2 + u_{\mathbb{Z},\mathbb{Y}}^2\right)\end{matrix}\right\}^T\begin{bmatrix}\mathfrak{Y}_T^{\mathbb{X}}\\ \mathfrak{Y}_T^{\mathbb{Y}}\end{bmatrix}\right)\mathrm{d}V, \tag{22}$$

$\boldsymbol{\mathfrak{Y}}_0 = \begin{bmatrix}\mathfrak{Y}_T^{\mathbb{X}}\\ \mathfrak{Y}_T^{\mathbb{Y}}\end{bmatrix}$ in Eq. (26). In the Green-Lagrange sense, the nonlinear strain vector

$$\boldsymbol{\mathcal{E}}_{\mathrm{nl}} = \left\{\begin{matrix}\dfrac{1}{2}(u_{\mathbb{X},\mathbb{X}}^2 + u_{\mathbb{Y},\mathbb{X}}^2 + u_{\mathbb{Z},\mathbb{X}}^2)\\ \dfrac{1}{2}(u_{\mathbb{X},\mathbb{Y}}^2 + u_{\mathbb{Y},\mathbb{Y}}^2 + u_{\mathbb{Z},\mathbb{Y}}^2)\end{matrix}\right\}$$

is intended. The second component of the virtual internal work caused by in-plane pre-thermal stresses in an element may be obtained by performing a few simple mathematical procedures as follows:

$$\delta\mathfrak{L}_{II} = \delta\boldsymbol{u}_{sj}^T\mathbf{K}_{II}^{\tau sij}(T_1)\boldsymbol{u}_{\tau i}, \tag{23}$$

where the second rigidity fundamental nucleus, $\mathbf{K}_{II}^{\tau sij}(T_1)$, is:

$$\mathbf{K}_{II}^{\tau sij}(T_1) = \left(\left(\int \mathfrak{Y}_T^{\mathbb{X}}\mathfrak{U}_{\tau}\mathfrak{U}_{s}\mathrm{d}\mathbb{Z}\int_{A_e}\mathfrak{H}_{i,\mathbb{X}}\mathfrak{H}_{j,\mathbb{X}}\mathrm{d}A\right) + \left(\int \mathfrak{Y}_T^{\mathbb{Y}}\mathfrak{U}_{\tau}\mathfrak{U}_{s}\mathrm{d}\mathbb{Z}\int_{A_e}\mathfrak{H}_{i,\mathbb{Y}}\mathfrak{H}_{j,\mathbb{Y}}\mathrm{d}A\right)\right)\mathbf{I}, \tag{24}$$

in which $\mathbf{I}$ is an identity matrix of rank three. The plane stress condition for the FG plates may be considered to determine the thermal buckling loads. It suggests that the in-plane pre-buckling stresses $\mathfrak{Y}_T^{\mathbb{X}}$ and $\mathfrak{Y}_T^{\mathbb{Y}}$ are calculated using Eq. (25) [63] and that $\mathfrak{Y}_T^{\mathbb{Z}} = 0$.

$$\mathfrak{Y}_T^{\mathbb{X}} = \mathfrak{Y}_T^{\mathbb{Y}} = -\frac{E(T(\mathbb{Z}),\mathbb{Z})\alpha(T(\mathbb{Z}),\mathbb{Z})T(\mathbb{Z})}{1-2\nu(T(\mathbb{Z}),\mathbb{Z})}. \tag{25}$$

It should be mentioned that the pre-buckling thermal stresses put the sandwich plates in a biaxial in-plane stress state and that Eq. (25) assumes that the plate is rigidly held in extension.

Additionally, the same process has been used to calculate the third portion of the virtual internal work completed by the auxetic foundation:

$$\delta\mathfrak{L}_{III} = \int_{A_e}(\delta\boldsymbol{u}_{sj}^T f_m^k)\mathrm{d}A. \tag{26}$$

in which the foundation is

$$f_m^k = \begin{bmatrix}0 & 0 & 0\\ 0 & 0 & 0\\ 0 & 0 & p_{\mathbb{Z}}\end{bmatrix}\begin{bmatrix}u_{\mathbb{X}_{\tau i}}\\ u_{\mathbb{Y}_{\tau i}}\\ u_{\mathbb{Z}_{\tau i}}\end{bmatrix}$$

applied at the coordinate $-\frac{h}{2}$.

The mathematical formulation of a Haber-Schaim foundation constructed from auxetic material inside the Cartesian coordinate system is expressed as follows [64]:

$$p_{\mathbb{Z}} = \left(K_w + \mathbb{D}_{AF}\nabla^4\right). \tag{27}$$

K_w, ν_{AF}, and h_{AF} are Winkler coefficient, Poisson's ratio of the auxetic foundation, and foundation plate thickness, respectively. Also, $\mathbb{D}_{AF}$ is equal to $\frac{E_{AF}h_{AF}^3}{12(1-\nu_{AF}^2)}$. The second component of the virtual internal work caused by auxetic foundation in an element may be obtained by performing a few simple mathematical procedures as follows:

$$\delta\mathfrak{L}_{III} = \delta\boldsymbol{u}_{sj}^T\mathbf{K}_{III}^{\tau sij}(T_1)\boldsymbol{u}_{\tau i}. \tag{28}$$

where $\mathbf{K}_{III}^{\tau sij}(T_1)$, which is called the third stiffness fundamental nucleus.

4. Thermal buckling load

The three main steps in the assembly process are creating the node matrix, the element matrix, and finally, the global stiffness matrices utilizing the nucleus matrices. The overall stiffness matrix is as follows $\mathbf{K}(T_1)$:

$$\mathbf{K}(T_1) = \mathbf{K}_I(T_1) + \mathbf{K}_{II}(T_1) + \mathbf{K}_{III}(T_1), \tag{29}$$

Since there are no external loads in this work, the plate's static equilibrium equation will be as follows:

$$\mathbf{K}(T_1).\boldsymbol{u} = 0. \tag{30}$$

The sequential linear problems (SLP) approach is used to solve the nonlinear equation (Eq. 30) [65]. This technique turns Eq. (30) into a linear equation by using two initial elements of the Taylor series at T_1^0 :

$$(\mathbf{K}(T_1^0) + (T_1 - T_1^0)\times\mathbf{K}'(T_1^0)).\boldsymbol{u} = 0, \tag{31}$$

Then, by assuming $\Delta T = T_1 - T_1^0$, Eq. (31) is rewritten as follows:

$$\mathbf{K}(T_1^0).\boldsymbol{u} = -\Delta T\mathbf{K}'(T_1^0).\boldsymbol{u}. \tag{32}$$

ΔT is an eigenvalue known as critical temperature differences, and Eq. (32) is an eigenvalue issue. The SLP approach may be used to address the eigenvalue issue. The current method's methodology for determining the critical temperature is shown in Figure 3.

5. Introducing deep neural networks to estimate thermal buckling analysis of sandwich plate with a FG-GOEAM face sheet surrounded by auxetic concrete foundation

The estimation of thermal buckling behavior in advanced composite structures, such as sandwich plates with functionally graded graphene origami-enabled auxetic metamaterial (FG-GOEAM) face sheets, represents a complex challenge due to the intricate interactions between materials, structural configurations, and thermal loads. Traditional analytical and numerical methods, while accurate, often require substantial computational resources and can be limited in handling nonlinearities and intricate material behaviors like those present in FG-GOEAM systems. Consequently, researchers have increasingly turned to deep neural networks (DNNs) as powerful tools for estimating thermal buckling in such advanced materials, leveraging DNNs' capacity for capturing complex patterns and relationships from large datasets. Deep neural networks, characterized by their multiple hidden layers and interconnected neurons, excel at recognizing

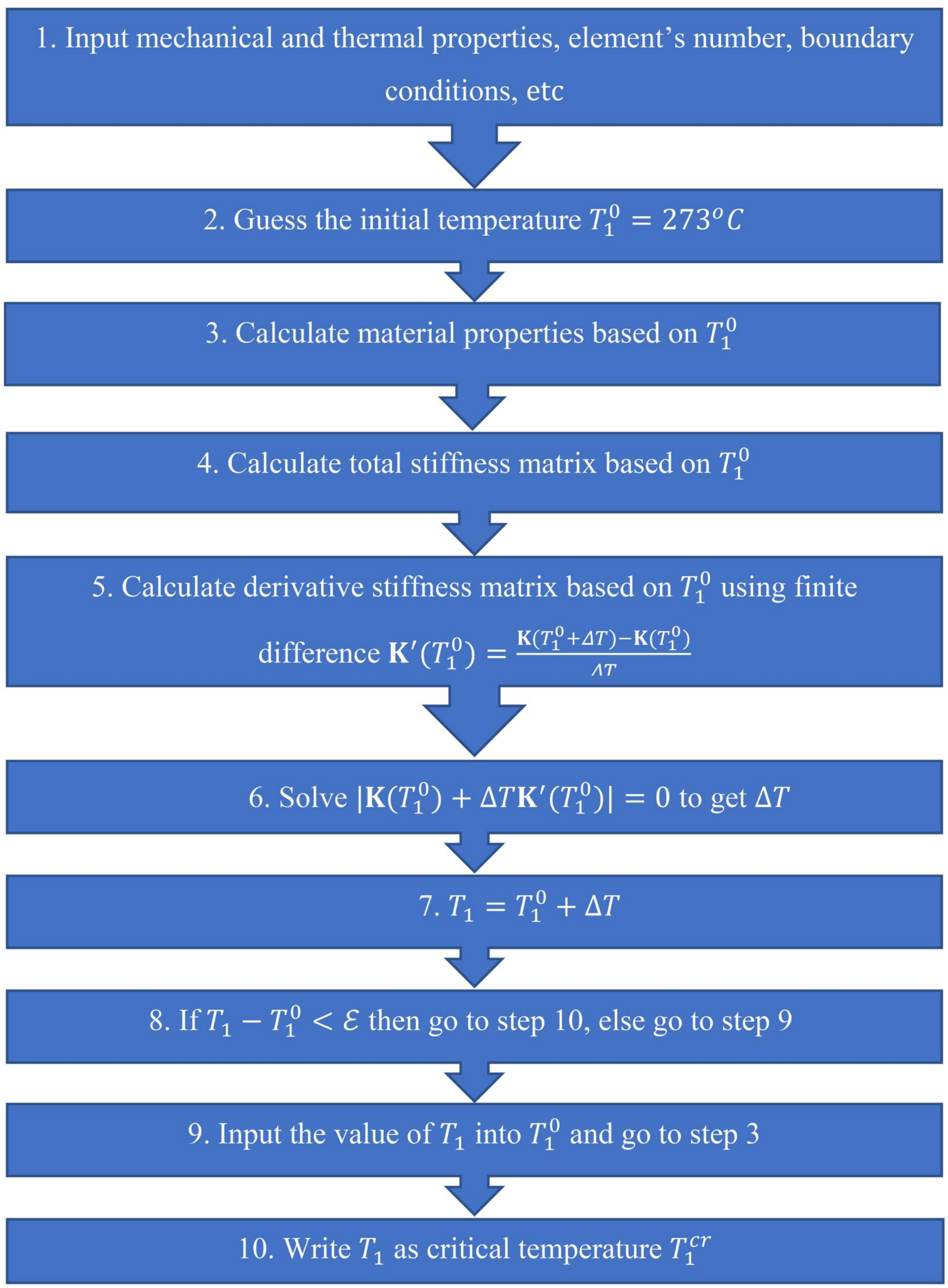

Figure 3. The current method's methodology for determining the critical temperature.

patterns in high-dimensional data, making them ideal for complex material and structural analyses. In the context of thermal buckling of FG-GOEAM-based sandwich plates, DNNs can be trained on datasets generated from finite element simulations or experimental studies, learning the relationships between inputs, such as plate geometry (e.g. aspect ratio \(a/h\)), weight fractions of FG-GOEAM, thermal loads, and boundary conditions, and the resulting critical buckling temperature differences. Once trained, a DNN can predict thermal buckling outcomes for new input scenarios with high accuracy and significantly lower computational costs than traditional methods. Implementing DNNs for thermal buckling analysis involves several key steps: data generation, model architecture selection, training, and validation. Data generation is typically achieved through a combination of finite element modeling (FEM) or experimental measurements, ensuring the dataset spans a wide range of configurations, weight fractions, and thermal loading conditions relevant to FG-GOEAM sandwich structures. Next, a suitable DNN architecture is selected, often involving deep feedforward networks or convolutional neural networks (CNNs) that are well-suited for capturing spatial dependencies and nonlinear behaviors. The DNN model is then trained by adjusting its weights and biases to minimize the prediction error against known outputs (i.e. critical buckling temperature differences). During training, optimization techniques, such as stochastic gradient descent (SGD) and regularization methods (e.g. dropout) are used to enhance the model's generalizability and prevent overfitting. Hyperparameter tuning—adjusting parameters like learning rate, batch size, and number of layers—ensures that the network reaches an optimal balance between accuracy and computational efficiency. Once trained, the model's performance is validated against a separate test dataset, confirming its predictive accuracy. The benefits of employing DNNs for thermal buckling analysis of FG-GOEAM sandwich plates are numerous. DNNs can perform rapid predictions, making them advantageous for real-time applications and parametric studies where multiple scenarios need to be evaluated. Additionally, DNNs can capture nonlinear interactions between thermal, mechanical, and material parameters that might be challenging to model analytically. This ability is particularly useful in FG-GOEAM structures, where the unique auxetic properties and graphene reinforcement introduce complex, multi-scale behaviors under thermal loading. In summary, DNNs offer an efficient, accurate, and adaptable method for estimating thermal buckling behavior in FG-GOEAM-based sandwich plates. By incorporating these models into thermal buckling analysis, researchers can explore a broader design space, optimize materials and structures, and accelerate the development of high-performance auxetic composites for applications requiring robust thermal stability. Figure 4 is a Python code using a deep neural network with Keras to estimate the thermal buckling temperature difference of a sandwich plate based on parameters like aspect ratio, weight fraction, and material properties. This code assumes you have a dataset with input features and target labels.

This code creates a simple feedforward neural network to predict the critical buckling temperature difference based on three input features. Replace X and Y with your actual dataset, and adjust parameters as needed.

6. Results and discussion

6.1. Validation

Table 1 provides a comparative analysis of the critical buckling temperature difference for simply supported functionally graded graphene platelet-reinforced composite (FG-GPLRC) square plates with varying width-to-thickness ratios and different functionally graded (FG) reinforcement patterns, specifically U-GPLRC and X-GPLRC configurations. The table presents critical buckling temperature differences calculated by the "Present" method, alongside values from Refs. [66, 67], to validate the accuracy and consistency of the current study's findings. The U-GPLRC and X-GPLRC represent two different configurations in which graphene platelets are distributed through the thickness of the plate. The critical buckling temperature difference values are presented for three width-to-thickness ratios, $b/h = 25$, $b/h = 35$, and $b/h = 45$, which offer insights into how the plate's aspect ratio affects thermal stability under different reinforcement patterns. For U-GPLRC plates, the critical temperature difference decreases as b/h increases, showing values of 32.527, 16.673, and 10.106 °C for b/h ratios of 25, 35, and 45, respectively, according to the present study. The values obtained from the present method are closely aligned with those from Refs. [66, 67], with only slight variations that indicate consistency across methods. This suggests that as the plate becomes thinner relative to its width, its resistance to thermal buckling decreases, necessitating lower temperature differences for buckling to occur. For X-GPLRC plates, a similar trend is observed, with critical buckling temperature differences of 39.708, 20.395, and 12.369 °C for b/h ratios of 25, 35, and 45, respectively. The results from Refs. [66, 67] again show minor discrepancies, supporting the reliability of the present findings. The X-GPLRC configuration shows slightly higher buckling resistance than U-GPLRC for each aspect ratio, indicating that the X-pattern provides enhanced thermal stability. Overall, Table 1 demonstrates the influence of GPL reinforcement patterns and aspect ratios on thermal buckling behavior in FG-GPLRC plates. The close agreement between the present study's results and those from previous studies validates the methodology used and highlights the advantages of X-GPLRC over U-GPLRC in enhancing thermal buckling resistance.

6.2. Parametric results

Figure 5 illustrates the impact of the FG-GOEAM layer thickness on the total plate thickness ratio (h_f/h) on the thermal buckling behavior of a sandwich plate structure. The graph displays two curves representing different configurations of the FG-GOEAM pattern and associated parameters influencing thermal buckling. The vertical axis shows

```
import numpy as np
from tensorflow.keras.models import Sequential
from tensorflow.keras.layers import Dense
# Sample dataset (replace with actual data)
X = np.random.rand(100, 3)  # Features: aspect ratio, weight fraction, material property
y = np.random.rand(100, 1)  # Target: critical temperature difference
# Build model
model = Sequential([Dense(64, activation='relu', input_shape=(3,)),
                Dense(32, activation='relu'),
                Dense(1)])
model.compile(optimizer='adam', loss='mse')
model.fit(X, y, epochs=100, batch_size=10, verbose=0)  # Train model
```

Figure 4. A Python code using a deep neural network with Keras to estimate the thermal buckling temperature difference of the current work.

Table 1. Comparing the critical buckling temperature difference for FG-GPLRC square plates that are simply supported and have varying FG patterns and width-to-thickness ratios.

		b/h		
Type	Method	25	35	45
U-GPLRC	Present	32.527	16.673	10.106
	Ref. [66]	32.539	16.679	10.109
	Ref. [67]	32.538	16.679	10.109
X-GPLRC	Present	39.708	20.395	12.369
	Ref. [66]	40.261	20.660	12.528
	Ref. [67]	40.261	20.659	12.527

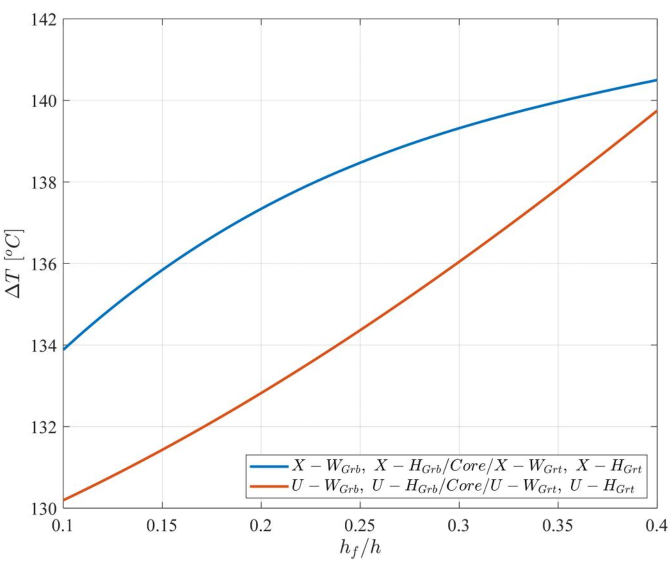

Figure 5. The influences of FG-GOEAM layer's thickness to plate thickness and FG-GOEAM's pattern on the thermal buckling information of the presented sandwich structure.

the critical temperature difference in degrees Celsius, which indicates the temperature threshold at which buckling occurs. The horizontal axis represents the h_f/h ratio, reflecting the relative thickness of the FG-GOEAM layer compared to the overall plate thickness. As h_f/h ratio increases, and the critical temperature difference also increases for both configurations, implying improved thermal stability with a thicker FG-GOEAM layer. The blue curve corresponds to a setup with higher thermal resistance, demonstrating a higher critical temperature difference than the red curve, which represents a less resistant configuration. This comparison highlights that both the FG-GOEAM layer thickness and pattern configuration significantly affect the sandwich

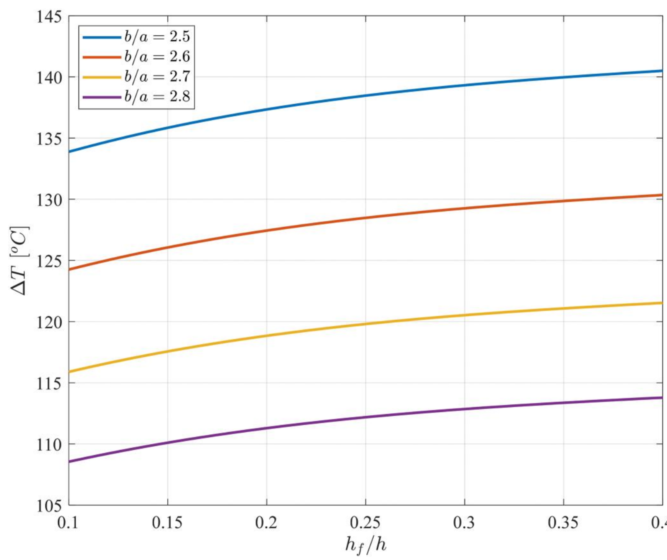

Figure 6. The influences of FG-GOEAM layer's thickness to plate thickness and b/a ratios on the thermal buckling information of the presented sandwich structure.

structure's thermal buckling performance. An increase in h_f/h ratio enhances the thermal buckling resistance, making the sandwich plate more resilient to thermal loads, which is essential for structural applications requiring high thermal stability.

Figure 6 depicts the effect of the thickness ratio of the FG-GOEAM layer to the total plate thickness and the aspect ratio on the thermal buckling performance of the sandwich structure. The vertical axis represents the critical temperature difference in degrees Celsius, indicating the temperature at which thermal buckling occurs, while the horizontal axis shows h_f/h ratio, the relative thickness of the FG-GOEAM layer. The graph includes four curves, each corresponding to a different b/a ratio (2.5, 2.6, 2.7, and 2.8). As h_f/h ratio increases, the critical temperature difference increases across all aspect ratios, showing that a thicker FG-GOEAM layer improves the structure's thermal buckling resistance. Among the curves, the configuration with $b/a = 2.5$ exhibits the highest critical temperature difference, while $b/a = 2.8$ has the lowest. This pattern indicates that lower aspect ratios result in better thermal stability under buckling loads. Overall, the data suggest that both h_f/h ratio and reducing b/a enhance thermal buckling resistance, which is crucial

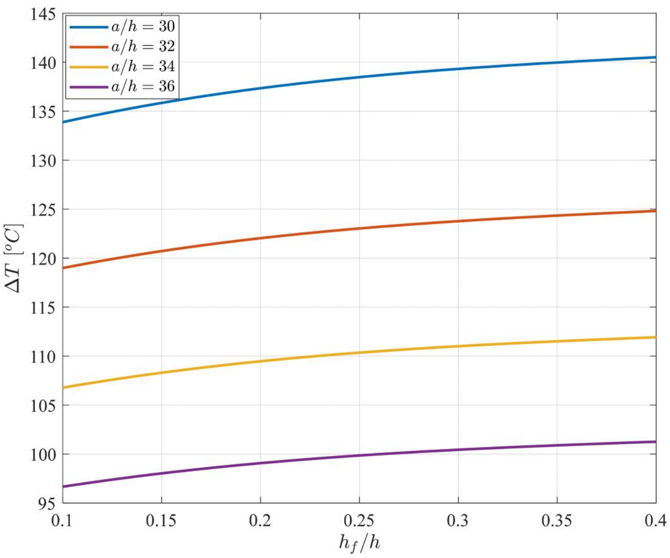

Figure 7. The influences of FG-GOEAM layer's thickness to plate thickness and a/h ratios on the thermal buckling information of the presented sandwich structure.

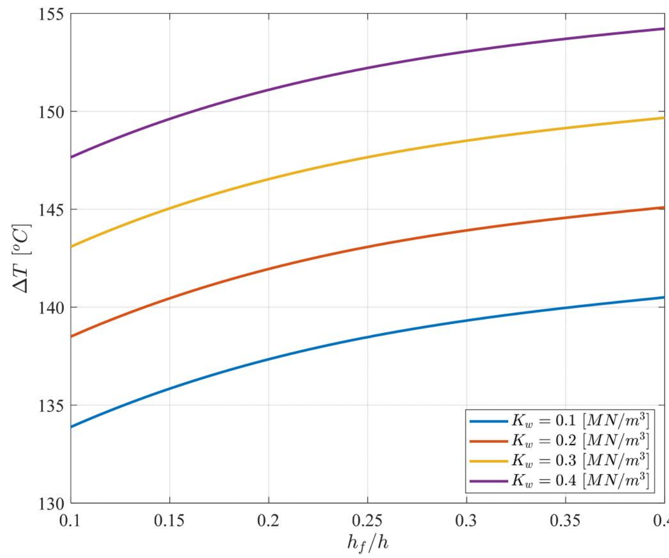

Figure 8. The influences of FG-GOEAM layer's thickness to plate thickness and Winkler foundation parameter on the thermal buckling information of the presented sandwich structure.

for applications requiring robust thermal performance in layered composite structures.

Figure 7 shows the influence of the thickness ratio of the FG-GOEAM layer to the total plate thickness and the plate slenderness ratio on the thermal buckling behavior of the sandwich structure. The vertical axis represents the critical temperature difference in degrees Celsius, indicating the temperature at which thermal buckling occurs, while the horizontal axis shows h_f/h ratio, the thickness ratio of the FG-GOEAM layer. The plot includes four curves, each representing a different slenderness ratio values of 30, 32, 34, and 36). Across all curves, an increase in h_f/h ratio leads to a higher critical temperature difference, suggesting that a thicker FG-GOEAM layer enhances thermal buckling resistance. Among the curves, the configuration with $a/h = 30$ demonstrates the highest critical temperature difference, while $a/h = 36$ shows the lowest. This trend indicates that plates with lower slenderness ratios (thicker plates) are more resistant to thermal buckling. Overall, the data reveal that increasing h_f/h ratio and decreasing a/h improve the thermal buckling resistance of the sandwich structure, making it more resilient to thermal loads. This is beneficial for structural applications that require high thermal stability in layered materials.

Figure 8 illustrates the impact of the thickness ratio (where h_f is the thickness of the FG-GOEAM layer, and h is the total plate thickness) and the Winkler foundation parameter on the thermal buckling temperature difference for the sandwich plate structure with FG-GOEAM face sheets. The figure shows that as h_f/h ratio increases, the thermal buckling temperature difference also increases, indicating enhanced thermal stability. This trend is consistent across all values of K_w, which represents the stiffness of the surrounding auxetic concrete foundation. Each curve corresponds to a different Winkler foundation parameter value, ranging from $K_w = 0.1[\mathrm{MN/m^3}]$ to $K_w = 0.4[\mathrm{MN/m^3}]$. Higher K_w values result in increased thermal buckling temperatures,

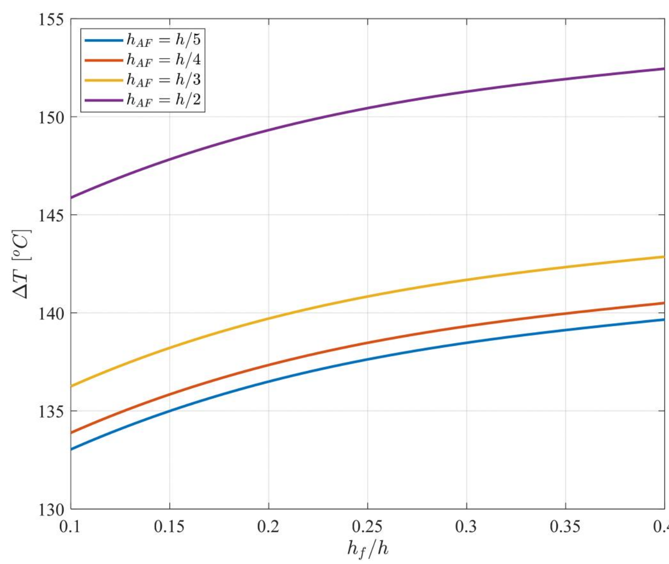

Figure 9. The influences of FG-GOEAM layer's thickness to plate thickness and auxetic foundation thickness on the thermal buckling information of the presented sandwich structure.

reflecting that a stiffer foundation enhances the thermal buckling resistance of the sandwich structure. Therefore, both an increase in the FG-GOEAM layer's thickness relative to the plate thickness and a stiffer foundation improve the structure's ability to withstand thermal loading before buckling. This behavior highlights the role of FG-GOEAM layer thickness and foundation stiffness in optimizing the thermal stability of sandwich plates in engineering applications.

Figure 9 presents the effects of the FG-GOEAM layer thickness to plate thickness ratio and the auxetic foundation thickness on the thermal buckling temperature difference of the sandwich structure with FG-GOEAM face sheets. The different curves represent varying values of h_{AF} relative to the total plate thickness, specifically $h_{AF} = h/5$, $h_{AF} = h/4$, $h_{AF} = h/2$, and $h_{AF} = h/2$. As h_f/h ratio increases, ΔT also rises across all values of h_{AF}, suggesting improved thermal stability with a thicker FG-GOEAM layer. Additionally, as the foundation thickness increases, the thermal buckling temperature difference also increases, indicating that a thicker auxetic foundation enhances the thermal buckling resistance of the sandwich structure. Thus, both a thicker FG-GOEAM layer and a thicker auxetic foundation contribute to a higher buckling temperature threshold, highlighting the role of these parameters in enhancing the thermal stability of the structure under thermal loading. This behavior is particularly relevant for applications requiring high thermal resistance in sandwich structures with auxetic materials.

Figure 10 illustrates the effect of the FG-GOEAM layer thickness to plate thickness ratio and the weight fraction of the FG-GOEAM, denoted as $W_{Grb} = W_{Grt}$, on the thermal buckling temperature difference of the sandwich structure with FG-GOEAM face sheets. The different curves represent varying FG-GOEAM weight fractions, specifically 0.2[wt%], 0.4[wt%], 0.6[wt%], and 0.8[wt%]. As the h_f/h ratio increases, the thermal buckling temperature also increases across all weight fractions, which indicates improved thermal stability with a thicker FG-GOEAM layer. Additionally, higher weight fractions of FG-GOEAM result in higher thermal buckling temperature values, suggesting that increasing the material concentration enhances the resistance of the sandwich structure to thermal buckling. This trend reflects the role of FG-GOEAM content in augmenting the thermal stability of the structure. Thus, both an increase in FG-GOEAM layer thickness and weight fraction contribute to enhancing the structure's thermal buckling resistance, which is beneficial for applications demanding high thermal resilience in sandwich plates with functionally graded auxetic metamaterials.

Figure 11 illustrates the effect of the FG-GOEAM layer's relative thickness and the hydrogen (H) atom coverage on the thermal buckling behavior of a sandwich plate with FG-GOEAM face sheets within an auxetic concrete foundation. The y-axis represents the critical temperature difference in degrees Celsius, indicating the threshold temperature difference at which thermal buckling occurs. The x-axis shows the ratio of FG-GOEAM layer thickness to total plate thickness, ranging from 0.1 to 0.4. Different curves represent varying H atom coverage levels from 25 to 100%, where each increase in H coverage is associated with a distinct color curve. Observing these curves, it is evident that for all levels of H coverage, the critical temperature difference initially increases with h_f/h, reaching a maximum before gradually decreasing. This trend highlights that there is an optimal FG-GOEAM layer thickness that maximizes the thermal stability of the structure for each H coverage level. Additionally, higher H coverage generally results in a lower critical temperature difference, indicating a reduction in thermal buckling resistance as H atom coverage increases. Consequently, the figure emphasizes the sensitivity of thermal buckling resistance to both the thickness ratio of FG-GOEAM layers and the extent of H coverage, suggesting that both parameters play critical roles in optimizing thermal stability in sandwich structures with auxetic foundations.

Figure 12 shows the impact of the FG-GOEAM weight fraction and the Winkler foundation stiffness coefficient on the thermal buckling response of the sandwich plate structure. Here, the y-axis represents the critical temperature difference in degrees Celsius, which indicates the temperature difference at which the plate will undergo thermal buckling. The x-axis denotes the weight fraction of the FG-GOEAM material in the structure, ranging from 0 to 1. Each curve corresponds to a different Winkler foundation stiffness coefficient, ranging from $K_w = 0.1$ to $0.4[MN/m^3]$. The figure reveals that an increase in both K_w and the FG-GOEAM weight fraction consistently elevates the critical temperature difference, indicating enhanced thermal stability. Specifically, for higher values of K_w, the critical temperature difference rises more significantly across the weight fraction range,

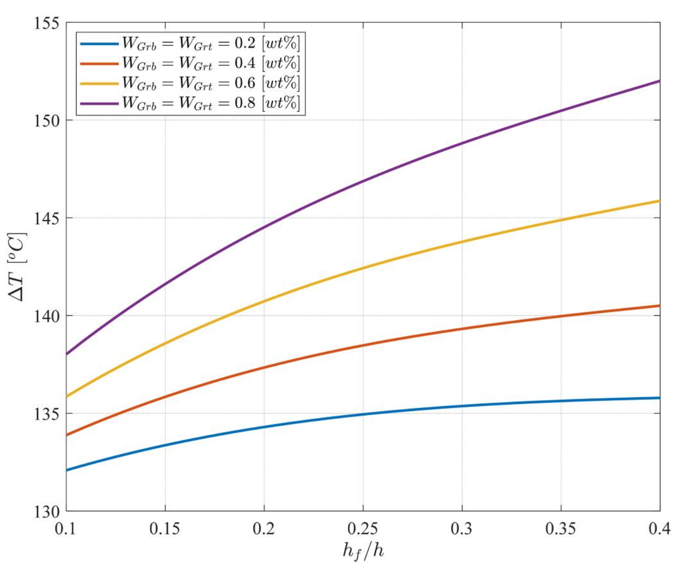

Figure 10. The influences of FG-GOEAM layer's thickness to plate thickness and FG-GOEAM weight fraction on the thermal buckling information of the presented sandwich structure.

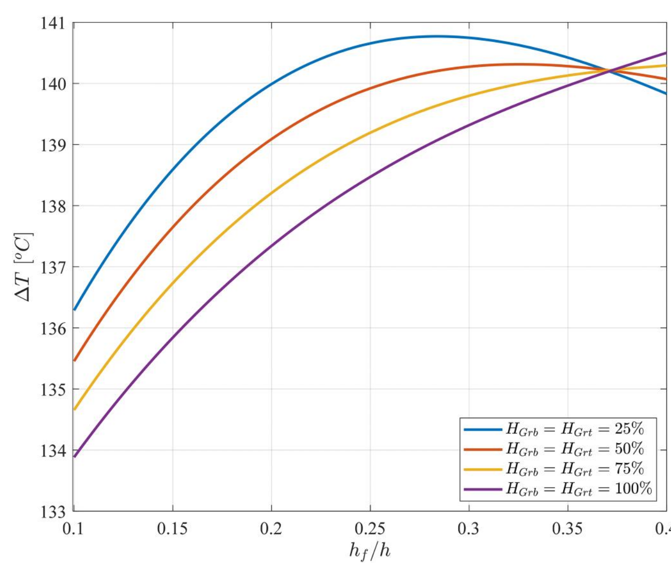

Figure 11. The influences of FG-GOEAM layer's thickness to plate thickness and H atom coverage on the thermal buckling information of the presented sandwich structure.

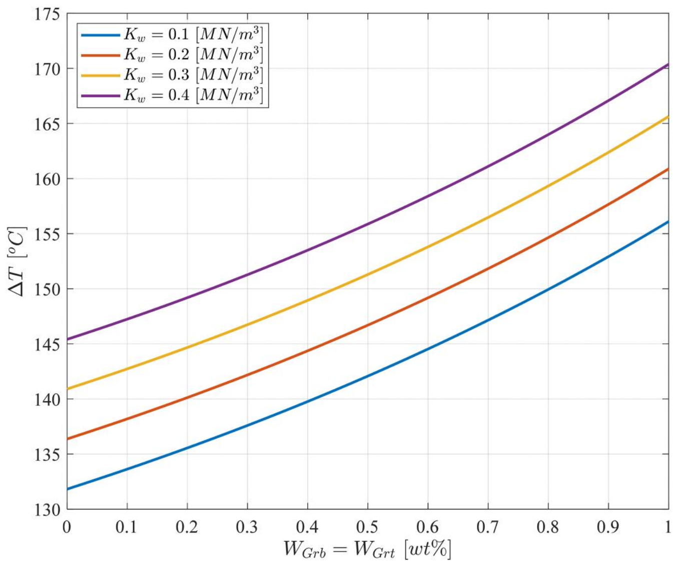

Figure 12. The influences of FG-GOEAM's weight fraction and Winkler coefficient on the thermal buckling information of the presented sandwich structure.

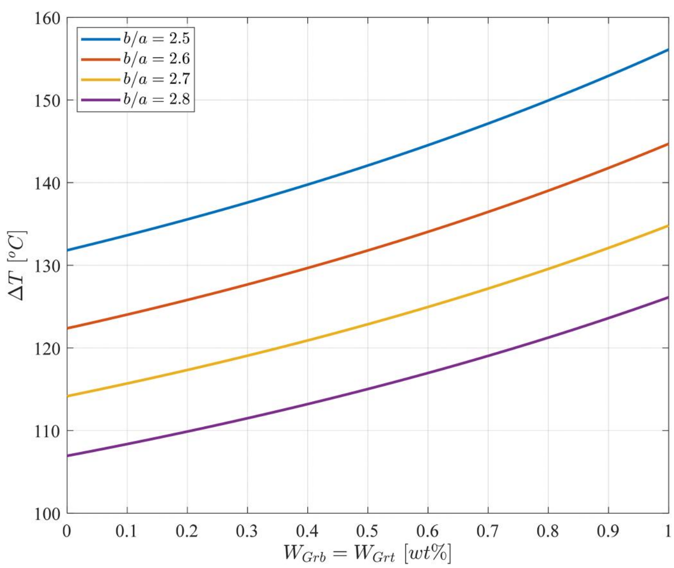

Figure 13. The influences of FG-GOEAM's weight fraction and b/a parameter on the thermal buckling information of the presented sandwich structure.

suggesting that the structural foundation stiffness plays a vital role in enhancing thermal buckling resistance. This trend implies that the sandwich structure's thermal stability can be optimized by carefully adjusting both the FG-GOEAM weight fraction and the stiffness of the Winkler foundation. Thus, the figure demonstrates the importance of these two parameters in improving the thermal buckling resistance of FG-GOEAM-based sandwich structures.

Figure 13 examines the effect of the FG-GOEAM weight fraction and the aspect ratio on the thermal buckling behavior of a sandwich plate structure. In this figure, the y-axis represents the critical temperature difference in degrees Celsius, marking the onset of thermal buckling, while the x-axis shows the weight fraction of FG-GOEAM material, ranging from 0 to 1. Each curve corresponds to a different aspect ratio, varying from 2.5 to 2.8. The figure demonstrates that for any fixed weight fraction, an increase in the aspect ratio results in a lower critical temperature difference. This indicates that higher aspect ratios lead to reduced thermal buckling resistance. Additionally, as the FG-GOEAM weight fraction increases, the critical temperature difference also rises across all aspect ratios, suggesting that higher FG-GOEAM content enhances the plate's thermal stability. The data imply that optimizing the FG-GOEAM weight fraction can improve thermal resistance, particularly at lower aspect ratios. This trend shows the combined influence of aspect ratio and FG-GOEAM content, emphasizing the importance of these parameters in designing sandwich structures that can withstand higher temperature gradients without buckling. Thus, by adjusting both the aspect ratio and FG-GOEAM weight fraction, the thermal stability of FG-GOEAM-based sandwich structures can be effectively controlled.

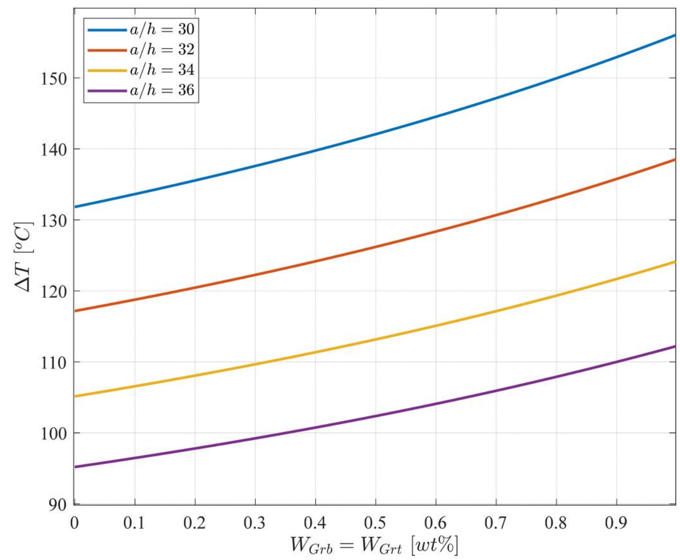

Figure 14. The influences of FG-GOEAM's weight fraction and a/h ratio on the thermal buckling information of the presented sandwich structure.

Figure 14 illustrates the relationship between the weight fraction of the FG-GOEAM layer, denoted as $W_{Grb} = W_{Grt}$, and the corresponding critical temperature difference required for thermal buckling in a sandwich plate structure with FG-GOEAM face sheets. The different colored curves represent varying aspect ratios, ranging from 30 to 36. The critical temperature difference is plotted on the y-axis, while the FG-GOEAM weight fraction is plotted on the x-axis. From the figure, it is observed that as the weight fraction of FG-GOEAM increases, the critical temperature difference also increases for all aspect ratios, indicating enhanced thermal stability. Additionally, for each incremental increase in the a/h ratio, the critical temperature difference decreases, implying that plates with a higher a/h ratio (thinner plates) are more susceptible to thermal buckling under lower temperature differences. This trend suggests that both the weight fraction of FG-GOEAM and the structural aspect ratio play significant roles in determining the thermal buckling resistance of the sandwich plate. Higher FG-GOEAM weight fractions and lower a/h ratios improve the thermal buckling resistance, making the structure more robust against temperature-induced deformation. This finding

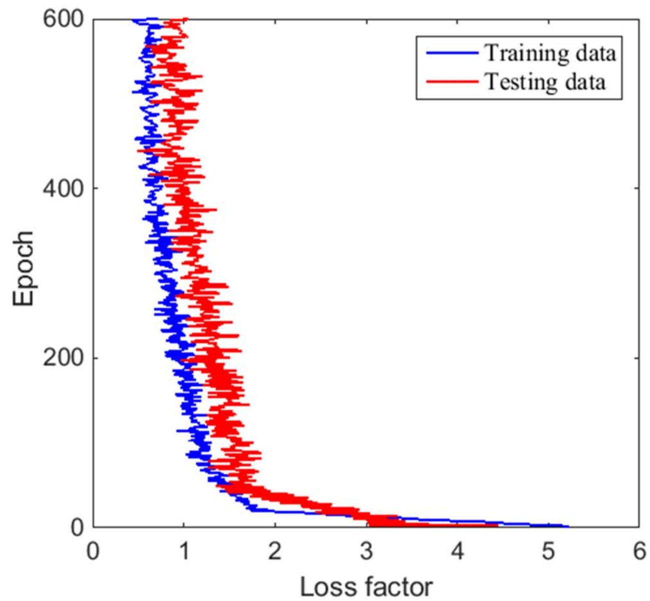

Figure 15. Loss factor against epoch for the presented deep neural networks.

highlights the potential of FG-GOEAM reinforcement to enhance thermal stability in sandwich structures with auxetic materials.

6.3. The results of the presented DNN algorithm

Figure 15 illustrates the training and testing loss convergence of a deep neural network (DNN) model used to estimate the critical buckling temperature difference in a functionally graded graphene origami-enabled auxetic metamaterial (FG-GOEAM) sandwich plate. The x-axis represents the "Loss factor," which quantifies the difference between the predicted and actual values of the critical temperature difference, while the y-axis represents the number of epochs, or iterations, of training. The training data loss is shown in blue, and the testing data loss is depicted in red. As shown in the figure, the loss factor for both training and testing data begins with relatively high values at the start of training (epoch 0) and decreases sharply during the initial epochs, indicating rapid convergence of the model. This rapid decrease signifies that the model quickly learns patterns in the data and adjusts its parameters to minimize the prediction error. The decreasing trend stabilizes around a loss factor of $\sim$0.5 after about 100 epochs, demonstrating that the model achieves convergence and no longer exhibits significant improvement with additional training. The close alignment between the training and testing loss curves suggests that the model generalizes well to new data, indicating minimal overfitting. This close fit implies that the DNN model effectively captures the underlying relationships between the input features (such as aspect ratio, weight fraction, and material properties) and the target output (critical buckling temperature difference) in FG-GOEAM sandwich plates. Overall, this figure demonstrates the efficiency of the DNN model in learning from training data while maintaining robust predictive accuracy on unseen testing data,

Table 2. DNN model's thermal buckling value for varying RMSE and a/b values.

		Predicted		
a/b	MR	$RMSE_{Train} = 0.4931$	$RMSE_{Train} = 0.5212$	$RMSE_{Train} = 0.6213$
1.5	156.613	120.947	149.176	156.811
2	131.663	107.885	120.721	131.662
2.5	88.677	60.5789	77.2502	88.7752
3	56.8134	47.1902	52.9016	57.0018
3.5	0.309	0.19748	0.29576	0.30886

Table 3. The DNN model's performance for thermal buckling value for different R^2 and W_{Grb}.

		Predicted		
$W_{Grb} = W_{Grt}(wt\%)$	MR	$R^2 = 0.9131$	$R^2 = 0.9421$	$R^2 = 0.9961$
0	76.9536	56.9707	72.0999	77.129
1	110.621	77.2502	94.7742	110.496
2	120.541	90.6389	112.762	120.527
3	175.851	126.728	149.889	175.975
4	211.021	161.418	200.488	211.178

thereby validating its effectiveness for thermal buckling analysis in advanced composite materials.

This section examines the effects of R^2 and RMSE on the results shown in Tables 2 and 3. It has been noted that more accurate responses are produced by higher RMSE and R^2 values. Therefore, it is recommended to use $R^2 = 0.9961$, RMSE $= 0.6213$, and 4580 samples when selecting the findings. The findings of the mathematical modeling are also shown in Mathematics findings (MR).

Tables 2 and 3 show how the existing structure's thermal buckling value varies with $W_{Grb} = W_{Grt}$ and a/b. Further details on this topic will be provided in the section that follows.

7. Conclusion

In conclusion, this study successfully applied CUF to analyze the thermal buckling behavior of sandwich plates with FG-GOEAM face sheets, supported by an auxetic concrete foundation. CUF, recognized for its flexibility in higher-order theory development, effectively captured the complex interactions between the FG-GOEAM layers and the auxetic foundation under thermal loads. By accurately modeling the material gradation and auxetic properties inherent in FG-GOEAM, CUF offered detailed insights into the thermal buckling responses of these advanced composite structures, providing a robust theoretical foundation for future analyses of similar configurations. To enhance computational efficiency without compromising accuracy, a DNN was implemented as a machine learning algorithm to predict critical buckling temperature differences, based on datasets generated from mathematics simulation. The DNN model demonstrated high predictive accuracy, validated through close agreement with CUF results across various parameter sets. By accurately learning the relationships between input parameters—such as material gradation, aspect ratio, and auxetic foundation properties—and critical buckling temperature, the DNN provided a rapid, reliable estimation tool that significantly reduced computational demands. The parametric studies revealed that FG-GOEAM sandwich plates exhibit superior thermal stability, influenced by both the aspect ratio and the auxetic foundation properties. Specifically, increasing the graphene origami content and optimizing the auxetic foundation enhanced the resistance of the sandwich plate to thermal buckling, underscoring the potential of FG-GOEAM materials in high-temperature applications. Additionally, the auxetic concrete foundation played a crucial role in stabilizing the structure, amplifying the thermal buckling resistance through its negative Poisson's ratio, which enhanced load distribution under thermal stress. This research contributed a novel, integrated approach that combines CUF-based high-fidelity modeling with DNN-driven machine learning for efficient, accurate thermal buckling analysis. The successful validation of the DNN model not only demonstrated the applicability of machine learning in advanced structural analysis but also highlighted its potential for reducing computational time in large-scale simulations. Overall, this study established a comprehensive framework for analyzing thermal buckling in FG-GOEAM structures, bridging advanced theoretical modeling and machine learning. These findings lay the groundwork for future research and applications of FG-GOEAM and auxetic materials in engineering fields that demand lightweight, thermally stable structures, such as aerospace, civil engineering, and materials science.

Disclosure statement

No potential conflict of interest was reported by the author(s).

Funding

The authors extend their appreciation to King Saud University, Saudi Arabia for funding this work through Researchers Supporting Project number (RSP2024R397), King Saud University, Riyadh, Saudi Arabia.

References

[1] E. Mohseni, A. Saidi, and M. Mohammadi, Bending-stretching analysis of thick functionally graded micro-plates using higher-order shear and normal deformable plate theory, Mech. Adv. Mater. Struct., vol. 24, no. 14, pp. 1221–1230, 2017. DOI: 10.1080/15376494.2016.1227503.

[2] Z.-Z. Wang, T. Wang, Y. Ding, and L. Ma, A simple refined plate theory for the analysis of bending, buckling and free vibration of functionally graded porous plates reinforced by graphene platelets, Mech. Adv. Mater. Struct., vol. 31, no. 8, pp. 1699–1716, 2024. DOI: 10.1080/15376494.2022.2141383.

[3] H.-S. Shen, X.-H. Huang, and J. Yang, Nonlinear bending of temperature-dependent FG-CNTRC laminated plates with negative Poisson's ratio, Mech. Adv. Mater. Struct., vol. 27, no. 13, pp. 1141–1153, 2020. DOI: 10.1080/15376494.2020.1716412.

[4] C. Lin, G. Pan, and M. Abbas, Introducing ANN-GP algorithm to estimate transient bending of the functionally graded graphene origami-enabled auxetic metamaterial structures, Mech. Adv. Mater. Struct., pp. 1–20, 2024. DOI: 10.1080/15376494.2024.2344020.

[5] A.G. Chanda and D. Punera, Porosity-dependent free vibration and transient responses of functionally graded composite plates employing higher order thickness stretching model, Mech. Adv. Mater. Struct., vol. 31, no. 7, pp. 1491–1516, 2024. DOI: 10.1080/15376494.2022.2138652.

[6] J. Najd, E. Zappino, E. Carrera, W. Harizi, and Z. Aboura, Optimal position and dimensions of embedded normal piezoelectric transducers, higher order plate models and experimental approach, Mech. Adv. Mater. Struct., pp. 1–12, 2024. DOI: 10.1080/15376494.2024.2342028.

[7] E. Carrera, and V. Zozulya, Carrera unified formulation (CUF) for the shells of revolution. Numerical evaluation, Mech. Adv. Mater. Struct., vol. 31, no. 7, pp. 1597–1619, 2024. DOI: 10.1080/15376494.2022.2140234.

[8] Z. Zhong, S. Chen, and E. Shang, Analytical solution of a functionally graded plate in cylindrical bending, Mech. Adv. Mater. Struct., vol. 17, no. 8, pp. 595–602, 2010. DOI: 10.1080/15376494.2010.517729.

[9] S.-R. Li, F. Zhang, and R.-G. Liu, Classical and homogenized expressions for the bending solutions of FGM plates based on the four variable plate theories, Mech. Adv. Mater. Struct., pp. 1–12, 2023.

[10] A. Belounar, S. Benmebarek, and L. Belounar, Strain based triangular finite element for plate bending analysis, Mech. Adv. Mater. Struct., vol. 27, no. 8, pp. 620–632, 2020. DOI: 10.1080/15376494.2018.1488310.

[11] R. Augello, A. Pagani, and E. Carrera, Analysis of plate reinforced by straight and curved stiffeners by using novel plate elements with refined through-the-thickness expansion, Mech. Adv. Mater. Struct., pp. 1–4, 2023. DOI: 10.1080/15376494.2023.2270794.

[12] E. Carrera, F. Miglioretti, and M. Petrolo, Accuracy of refined finite elements for laminated plate analysis, Compos. Struct., vol. 93, no. 5, pp. 1311–1327, 2011. DOI: 10.1016/j.compstruct.2010.11.007.

[13] E. Carrera, M.D. Demirbas, and R. Augello, Evaluation of stress distribution of isotropic, composite, and FG beams with different geometries in nonlinear regime via Carrera-Unified Formulation and Lagrange polynomial expansions, Appl. Sci., vol. 11, no. 22, pp. 10627, 2021. DOI: 10.3390/app112210627.

[14] M. Burkov and A. Eremin, Evaluation of fracture toughness of hybrid CNT/CFRP composites, Mech. Adv. Mater. Struct., vol. 30, no. 14, pp. 2872–2881, 2023. DOI: 10.1080/15376494.2022.2064569.

[15] K. Bendine, F. Boukhoulda, B. Haddag, and M. Nouari, Active vibration control of composite plate with optimal placement of piezoelectric patches, Mech. Adv. Mater. Struct., vol. 26, no. 4, pp. 341–349, 2019. DOI: 10.1080/15376494.2017.1387324.

[16] M.M. Abdel-Mottaleb, A. Mohamed, S.A. Karim, T.A. Osman, and A. Khattab, Preparation, characterization, and mechanical properties of polyacrylonitrile (PAN)/graphene oxide (GO) nanofibers, Mech. Adv. Mater. Struct., vol. 27, no. 4, pp. 346–351, 2020. DOI: 10.1080/15376494.2018.1473535.

[17] B. Abuteir, E. Harkati, D. Boutagouga, S. Mamouri, and K. Djeghaba, Thermo-mechanical nonlinear transient dynamic and Dynamic-Buckling analysis of functionally graded material shell structures using an implicit conservative/decaying time integration scheme, Mech. Adv. Mater. Struct., vol. 29, no. 27, pp. 5773–5792, 2022. DOI: 10.1080/15376494.2021.1964115.

[18] G. Chen, J. Chen, and J. Teng, Behaviour of FRP-to-concrete interfaces between two adjacent cracks: a numerical investigation on the effect of bondline damage, Constr. Build. Mater., vol. 28, no. 1, pp. 584–591, 2012. DOI: 10.1016/j.conbuildmat.2011.08.074.

[19] M. Amini, M. Soleimani, A. Altafi, and A. Rastgoo, Effects of geometric nonlinearity on free and forced vibration analysis of moderately thick annular functionally graded plate, Mech. Adv. Mater. Struct., vol. 20, no. 9, pp. 709–720, 2013. DOI: 10.1080/15376494.2012.676711.

[20] H.-T. Thai, T.-K. Nguyen, T.P. Vo, and J. Lee, Analysis of functionally graded sandwich plates using a new first-order shear deformation theory, Eur. J. Mech. A/Solids, vol. 45, pp. 211–225, 2014. DOI: 10.1016/j.euromechsol.2013.12.008.

[21] T.-K. Nguyen, V.-H. Nguyen, T. Chau-Dinh, T.P. Vo, and H. Nguyen-Xuan, Static and vibration analysis of isotropic and functionally graded sandwich plates using an edge-based MITC3 finite elements, Compos. Part B Eng., vol. 107, pp. 162–173, 2016. DOI: 10.1016/j.compositesb.2016.09.058.

[22] F.Z. Zaoui, D. Ouinas, and A. Tounsi, New 2D and quasi-3D shear deformation theories for free vibration of functionally graded plates on elastic foundations, Compos. Part B Eng., vol. 159, pp. 231–247, 2019. DOI: 10.1016/j.compositesb.2018.09.051.

[23] A. Neves, A. Ferreira, E. Carrera, M. Cinefra, R. Jorge, and C. Soares, Buckling analysis of sandwich plates with functionally graded skins using a new quasi-3D hyperbolic sine shear deformation theory and collocation with radial basis functions, Z. Angew. Math. Mech., vol. 92, no. 9, pp. 749–766, 2012. DOI: 10.1002/zamm.201100186.

[24] E. Carrera, A class of two-dimensional theories for anisotropic multilayered plates analysis, Atti Accad. Sci. Torino Classe Sci. Fisiche Mat. Nat., vol. 19, pp. 1–39, 1995.

[25] E. Carrera, Mixed layer-wise models for multilayered plates analysis, Compos. Struct., vol. 43, no. 1, pp. 57–70, 1998. DOI: 10.1016/S0263-8223(98)00097-X.

[26] E. Carrera, Developments, ideas, and evaluations based upon Reissner's Mixed Variational Theorem in the modeling of multilayered plates and shells, Appl. Mech. Rev., vol. 54, no. 4, pp. 301–329, 2001. DOI: 10.1115/1.1385512.

[27] E. Carrera, Theories and finite elements for multilayered plates and shells: a unified compact formulation with numerical assessment and benchmarking, Archiv. Comput. Methods Eng., vol. 10, no. 3, pp. 215–296, 2003. DOI: 10.1007/BF02736224.

[28] E. Carrera and B. Kröplin, Zigzag and interlaminar equilibria effects in large-deflection and postbuckling analysis of multilayered plates, Mech. Adv. Mater. Struct., vol. 4, no. 1, pp. 69–94, 1997. DOI: 10.1080/10759419708945875.

[29] E. Carrera, Transverse normal strain effect on thermal stress analysis of homogeneous and layered plates, AIAA J., vol. 43, no. 10, pp. 2232–2242, 2005. DOI: 10.2514/1.11230.

[30] A. Robaldo, E. Carrera, and A. Benjeddou, A unified formulation for finite element analysis of piezoelectric adaptive plates, Comput. Struct., vol. 84, no. 22–23, pp. 1494–1505, 2006. DOI: 10.1016/j.compstruc.2006.01.029.

[31] E. Carrera and A. Pagani, Free vibration analysis of civil engineering structures by component-wise models, J. Sound Vib., vol. 333, no. 19, pp. 4597–4620, 2014. DOI: 10.1016/j.jsv.2014.04.063.

[32] C. Qianying, X. Zeyang, W. Qingyou, L. Lili, W. Zhigang, W. Zhanjun, and L. Ling, Molding simulation of airfoil foam sandwich structure and interference optimization of foam-core, Chin. J. Aeronaut., vol. 37, no. 10, pp. 325–338, 2024.

[33] C. Yang, Z. Li, P. Xu, and H. Huang, Recognition and optimisation method of impact deformation patterns based on point cloud and deep clustering: applied to thin-walled tubes, J. Ind. Inform. Integr., vol. 40, pp. 100607, 2024. DOI: 10.1016/j.jii.2024.100607.

[34] Z. Wang, Y. Xiang, S. Zhang, X. Liu, J. Ma, J. Tan, and L. Wang, Physics-informed springback prediction of 3D aircraft tubes with six-axis free-bending manufacturing, Aerosp. Sci. Technol., vol. 147, pp. 109022, 2024. DOI: 10.1016/j.ast.2024.109022.

[35] S. Fan, T. He, W. Li, C. Zeng, P. Chen, L. Chen, and J. Shu, Machine learning-based classification of quality grades for concrete vibration behaviour, Autom. Constr., vol. 167, pp. 105694, 2024. DOI: 10.1016/j.autcon.2024.105694.

[36] K. Liu, S. Zong, Y. Li, Z. Wang, Z. Hu, and Z. Wang, Structural response of the U-type corrugated core sandwich panel used in ship structures under the lateral quasi-static compression load, Mar. Struct., vol. 84, pp. 103198, 2022. DOI: 10.1016/j.marstruc.2022.103198.

[37] X. Long, K. Chong, Y. Su, C. Chang, and L. Zhao, Meso-scale low-cycle fatigue damage of polycrystalline nickel-based alloy by crystal plasticity finite element method, Int. J. Fatigue, vol. 175, pp. 107778, 2023. DOI: 10.1016/j.ijfatigue.2023.107778.

[38] X. Long, Z. Shen, J. Li, R. Dong, M. Liu, Y. Su, and C. Chen, Size effect of nickel-based single crystal superalloy revealed by nanoindentation with low strain rates, J. Mater. Res. Technol., vol. 29, pp. 2437–2447, 2024. DOI: 10.1016/j.jmrt.2024.01.279.

[39] Y. Wang and O. Sigmund, Multi-material topology optimization for maximizing structural stability under thermo-mechanical loading, Comput. Methods Appl. Mech. Eng., vol. 407, pp. 115938, 2023. DOI: 10.1016/j.cma.2023.115938.

[40] B. Liu, H. Yang, and S. Karekal, Effect of water content on argillization of mudstone during the tunnelling process, Rock Mech. Rock Eng., vol. 53, no. 2, pp. 799–813, 2020. DOI: 10.1007/s00603-019-01947-w.

[41] H. Yang, C. Chen, J. Ni, and S. Karekal, A hyperspectral evaluation approach for quantifying salt-induced weathering of sandstone, Sci. Total Environ., vol. 885, pp. 163886, 2023. DOI: 10.1016/j.scitotenv.2023.163886.

[42] H. Yang, K. Song, and J. Zhou, Automated recognition model of geomechanical information based on operational data of tunneling boring machines, Rock Mech. Rock Eng., vol. 55, no. 3, pp. 1499–1516, 2022. DOI: 10.1007/s00603-021-02723-5.

[43] H. Yang, J. Ni, C. Chen, and Y. Chen, Weathering assessment approach for building sandstone using hyperspectral imaging technique, Herit. Sci., vol. 11, no. 1, pp. 70, 2023. DOI: 10.1186/s40494-023-00914-7.

[44] C. Chen, H. Yang, K. Song, D. Liang, Y. Zhang, and J. Ni, Dissolution feature differences of carbonate rock within hydrofluctuation belt located in the Three Gorges Reservoir Area, Eng. Geol., vol. 327, pp. 107362, 2023. DOI: 10.1016/j.enggeo.2023.107362.

[45] K. Song, H. Yang, D. Liang, L. Chen, and M. Jaboyedoff, Step-like displacement prediction and failure mechanism analysis of slow-moving reservoir landslide, J. Hydrol., vol. 628, pp. 130588, 2024. DOI: 10.1016/j.jhydrol.2023.130588.

[46] D. Hu, H. Sun, P. Mehrabi, Y.A. Ali, and M. Al-Razgan, Application of artificial intelligence technique in optimization and prediction of the stability of the walls against wind loads in building design, Mech. Adv. Mater. Struct., vol. 31, no. 19, pp. 4755–4772, 2024. DOI: 10.1080/15376494.2023.2206208.

[47] J. Wu, Y. Yang, P. Mehrabi, and E.A. Nasr, Efficient machine-learning algorithm applied to predict the transient shock reaction of the elastic structure partially rested on the viscoelastic substrate, Mech. Adv. Mater. Struct., vol. 31, no. 16, pp. 3700–3724, 2024. DOI: 10.1080/15376494.2023.2183289.

[48] S. Han, D. Zheng, B. Mehdizadeh, E.A. Nasr, M.U. Khandaker, M. Salman, and P. Mehrabi, Sustainable design of self-consolidating green concrete with partial replacements for cement through neural-network and fuzzy technique, Sustainability, vol. 15, no. 6, pp. 4752, 2023. DOI: 10.3390/su15064752.

[49] S. Han, Z. Zhu, M. Mortazavi, A.M. El-Sherbeeny, and P. Mehrabi, Analytical assessment of the structural behavior of a specific composite floor system at elevated temperatures using a newly developed hybrid intelligence method, Buildings, vol. 13, no. 3, pp. 799, 2023. DOI: 10.3390/buildings13030799.

[50] E. Taheri, P. Mehrabi, S. Rafiei, and B. Samali, Numerical evaluation of the upright columns with partial reinforcement along with the utilisation of neural networks with combining feature-selection method to predict the load and displacement, Appl. Sci., vol. 11, no. 22, pp. 11056, 2021. DOI: 10.3390/app112211056.

[51] J. Liu, M. Mohammadi, Y. Zhan, P. Zheng, M. Rashidi, and P. Mehrabi, Utilizing artificial intelligence to predict the superplasticizer demand of self-consolidating concrete incorporating pumice, slag, and fly ash powders, Materials, vol. 14, no. 22, pp. 6792, 2021. DOI: 10.3390/ma14226792.

[52] E. Taheri, A. Firouzianhaji, P. Mehrabi, B. Vosough Hosseini, and B. Samali, Experimental and numerical investigation of a method for strengthening cold-formed steel profiles in bending,

Appl. Sci., vol. 10, no. 11, pp. 3855, 2020. DOI: 10.3390/app10113855.

[53] Y. Feng, M. Mohammadi, L. Wang, M. Rashidi, and P. Mehrabi, Application of artificial intelligence to evaluate the fresh properties of self-consolidating concrete, Materials, vol. 14, no. 17, pp. 4885, 2021. DOI: 10.3390/ma14174885.

[54] A. Firouzianhaji, N. Usefi, B. Samali, and P. Mehrabi, Shake table testing of standard cold-formed steel storage rack, Appl. Sci., vol. 11, no. 4, pp. 1821, 2021. DOI: 10.3390/app11041821.

[55] P. Mehrabi, S. Honarbari, S. Rafiei, S. Jahandari, and M. Alizadeh Bidgoli, Seismic response prediction of FRC rectangular columns using intelligent fuzzy-based hybrid metaheuristic techniques, J. Amb. Intell. Hum. Comput., vol. 12, no. 11, pp. 10105–10123, 2021. DOI: 10.1007/s12652-020-02776-4.

[56] E. Taheri, A. Firouzianhaji, N. Usefi, P. Mehrabi, H. Ronagh, and B. Samali, Investigation of a method for strengthening perforated cold-formed steel profiles under compression loads, Appl. Sci., vol. 9, no. 23, pp. 5085, 2019. DOI: 10.3390/app9235085.

[57] P. Mehrabi, M. Shariati, K. Kabirifar, M. Jarrah, H. Rasekh, N.T. Trung, A. Shariati, and S. Jahandari, Effect of pumice powder and nano-clay on the strength and permeability of fiber-reinforced pervious concrete incorporating recycled concrete aggregate, Constr. Build. Mater., vol. 287, pp. 122652, 2021. DOI: 10.1016/j.conbuildmat.2021.122652.

[58] A. Toghroli, P. Mehrabi, M. Shariati, N.T. Trung, S. Jahandari, and H. Rasekh, Evaluating the use of recycled concrete aggregate and pozzolanic additives in fiber-reinforced pervious concrete with industrial and recycled fibers, Constr. Build. Mater., vol. 252, pp. 118997, 2020. DOI: 10.1016/j.conbuildmat.2020.118997.

[59] Y. Qiu and J. Wang, A machine learning approach to credit card customer segmentation for economic stability, Presented at the Proceedings of the 4th International Conference on Economic Management and Big Data Applications, ICEMBDA 2023, Tianjin, China, October 27–29, 2023, 2024.

[60] Y. Qiu, Estimation of tail risk measures in finance: Approaches to extreme value mixture modeling, Diss., Johns Hopkins University, 2019.

[61] S. Zhao, Y. Zhang, Y. Zhang, J. Yang, and S. Kitipornchai, Vibrational characteristics of functionally graded graphene origami-enabled auxetic metamaterial beams based on machine learning assisted models, Aerosp. Sci. Technol., vol. 130, pp. 107906, 2022. DOI: 10.1016/j.ast.2022.107906.

[62] S. Zhao, Y. Zhang, Y. Zhang, W. Zhang, J. Yang, and S. Kitipornchai, Genetic programming-assisted micromechanical models of graphene origami-enabled metal metamaterials, Acta Mater., vol. 228, pp. 117791, 2022. DOI: 10.1016/j.actamat.2022.117791.

[63] F. Moleiro, J.F.A. Madeira, E. Carrera, and A. Ferreira, Thermo-mechanical design optimization of symmetric and non-symmetric sandwich plates with ceramic-metal-ceramic functionally graded core to minimize stress, deformation and mass, Compos. Struct., vol. 276, pp. 114496, 2021. DOI: 10.1016/j.compstruct.2021.114496.

[64] A. Behravan-Rad and M. Jafari, Hygroelasticity analysis of an elastically restrained functionally graded porous metamaterial circular plate resting on an auxetic material circular plate, Appl. Math. Mech. Engl. Ed., vol. 41, no. 9, pp. 1359–1380, 2020. DOI: 10.1007/s10483-020-2651-7.

[65] C. Campos and J.E. Roman, NEP: a module for the parallel solution of nonlinear eigenvalue problems in SLEPc, ACM Trans. Math. Softw., vol. 47, no. 3, pp. 1–29, 2021. DOI: 10.1145/3447544.

[66] H. Wu, S. Kitipornchai, and J. Yang, Thermal buckling and postbuckling of functionally graded graphene nanocomposite plates, Mater. Des., vol. 132, pp. 430–441, 2017. DOI: 10.1016/j.matdes.2017.07.025.

[67] Y. Kiani, NURBS-based thermal buckling analysis of graphene platelet reinforced composite laminated skew plates, J. Therm. Stresses, vol. 43, no. 1, pp. 90–108, 2020. DOI: 10.1080/01495739.2019.1673687.